

Geochemistry, Geophysics, Geosystems



RESEARCH ARTICLE

10.1029/2022GC010718

Key Points:

- Weakly explosive water-lava interaction boiled Kīlauea's summit crater lake in 90 min and created an 11–13 km high, ash-poor plume
- The water-rich plume produced multiple lightning flashes generated by hydrometeor charging microphysics
- Lava supplied heat to the plume via boiling without contributing mass, which led to a taller plume than expected

Supporting Information:

Supporting Information may be found in the online version of this article.

Correspondence to:

R. C. Cahalan, rcahalan@usgs.gov

Citation:

Cahalan, R. C., Mastin, L. G., Van Eaton, A. R., Hurwitz, S., Smith, A. B., Dufek, J., et al. (2023). Dynamics of the December 2020 ash-poor plume formed by lava-water interaction at the summit of Kīlauea Volcano, Hawai'i. *Geochemistry, Geophysics, Geosystems*, 24, e2022GC010718. https://doi.org/10.1029/2022GC010718

Received 26 SEP 2022 Accepted 6 FEB 2023

© 2023 The Authors. This article has been contributed to by U.S. Government employees and their work is in the public domain in the USA.

This is an open access article under the terms of the Creative Commons Attribution License, which permits use, distribution and reproduction in any medium, provided the original work is properly cited.

Dynamics of the December 2020 Ash-Poor Plume Formed by Lava-Water Interaction at the Summit of Kīlauea Volcano, Hawai'i

Ryan C. Cahalan¹, Larry G. Mastin¹, Alexa R. Van Eaton¹, Shaul Hurwitz², Adam B. Smith³, Josef Dufek⁴, Stephen A. Solovitz⁵, Matt Patrick⁶, Johanne Schmith⁶, Carolyn Parcheta⁶, Weston A. Thelen¹, and Drew T. Downs⁶

¹Cascades Volcano Observatory, U.S. Geological Survey, Vancouver, WA, USA, ²California Volcano Observatory, U.S. Geological Survey, Moffett Field, CA, USA, ³Gemini Observatory/NSF's NOIRLab, Hilo, HI, USA, ⁴Department of Earth Science, University of Oregon, Eugene, OR, USA, ⁵Washington State University Vancouver, Vancouver, WA, USA, ⁶U.S. Geological Survey, Hawaiian Volcano Observatory, Hilo, HI, USA

Abstract On 20 December 2020, after more than 2 years of quiescence at Kīlauea Volcano, Hawai'i, renewed volcanic activity in the summit crater caused boiling of the water lake over a period of ~90 min. The resulting water-rich, electrified plume rose to 11-13 km above sea level, which is among the highest plumes on record for Kīlauea. Although conventional models would infer a high mass flux from explosive magma-water interaction, the plume was not associated with an infrasound signal indicative of "explosive" activity, nor did it produce a measurable ash-fall deposit. We use multisensor data to characterize lava-water interaction and plume generation during this opening phase of the 2020-21 eruption. Satellite, weather radar, and eyewitness observations revealed that the plume was rich in water vapor and hydrometeors but transported less ash than expected from its maximum height. Volcanic lightning flashes detected by ground-based cameras were confined to freezing altitudes of the upper cloud, suggesting that the ice formation drove the electrification of this plume. The low acoustic energy from lava-water interaction points to a weakly explosive style of hydrovolcanism. Heat transfer calculations show that the lava to water heat flux was sufficient to boil the lake within 90 min. Limited mixing of lava and water inhibited major steam explosions and fine fragmentation. Results from one-dimensional plume modeling suggest that the models may underpredict plume height due to overestimation of crosswind air-entrainment. Our findings shed light on an unusual style of volcanism in which weakly explosive lava-water interaction generated an outsized plume.

Plain Language Summary On 20 December 2020, after more than 2 years without an eruption at Kīlauea Volcano, lava erupted through the debris along the summit crater wall and flowed downslope into a hot, acidic water lake. The lava quickly heated and boiled the water, generating a volcanic cloud or plume that reached 11–13 km above sea level, among the highest plumes on record for Kīlauea. After 90 min, the lake had boiled away, leaving behind a new, growing lava lake. In this study, we investigated the processes that occurred during the interaction between the lava and the water lake and the tall plume that developed. Based on observations from weather radar, eyewitnesses, camera footage, acoustic measurements, and numerical modeling, we show the following: (a) interaction between the lava and water did not cause explosions, (b) the plume contained very little ash but carried abundant water vapor that formed ice at higher altitudes, which created lightning, and (c) heat transfer from lava to the water caused the plume to rise much higher than expected for an ash-poor eruption.

1. Introduction

The appearance of a water lake in Kīlauea's Halema'uma'u Crater (Figure 1) in mid-July 2019 reawakened concerns of violent lava-water interaction when eruptive activity returned to the volcano's summit (Nadeau et al., 2020).

Although Kīlauea is best known for its effusive volcanism, evidence from tephra deposits and native Hawaiian oral traditions indicates that violent lava-water interactions have occurred in Kīlauea's past (Mastin, 1997; Mastin et al., 2004; Swanson & Houghton, 2019; Swanson et al., 2014). For example, the Keanakāko'i Tephra, predominantly composed of layers of phreatic and phreatomagmatic ejecta that include numerous pyroclastic surge

CAHALAN ET AL. 1 of 23

1525/2027, 2023, 3, Downloaded from https://agupubs.onlinelibrary.wiley.com/doi/10.1029/2023CC010718, Wiley Online Library on [16/03/2023], See the Terms and Conditions (https://onlinelibrary.wiley.com/terms-and-conditions) on Wiley Online Library for rules of use; OA article

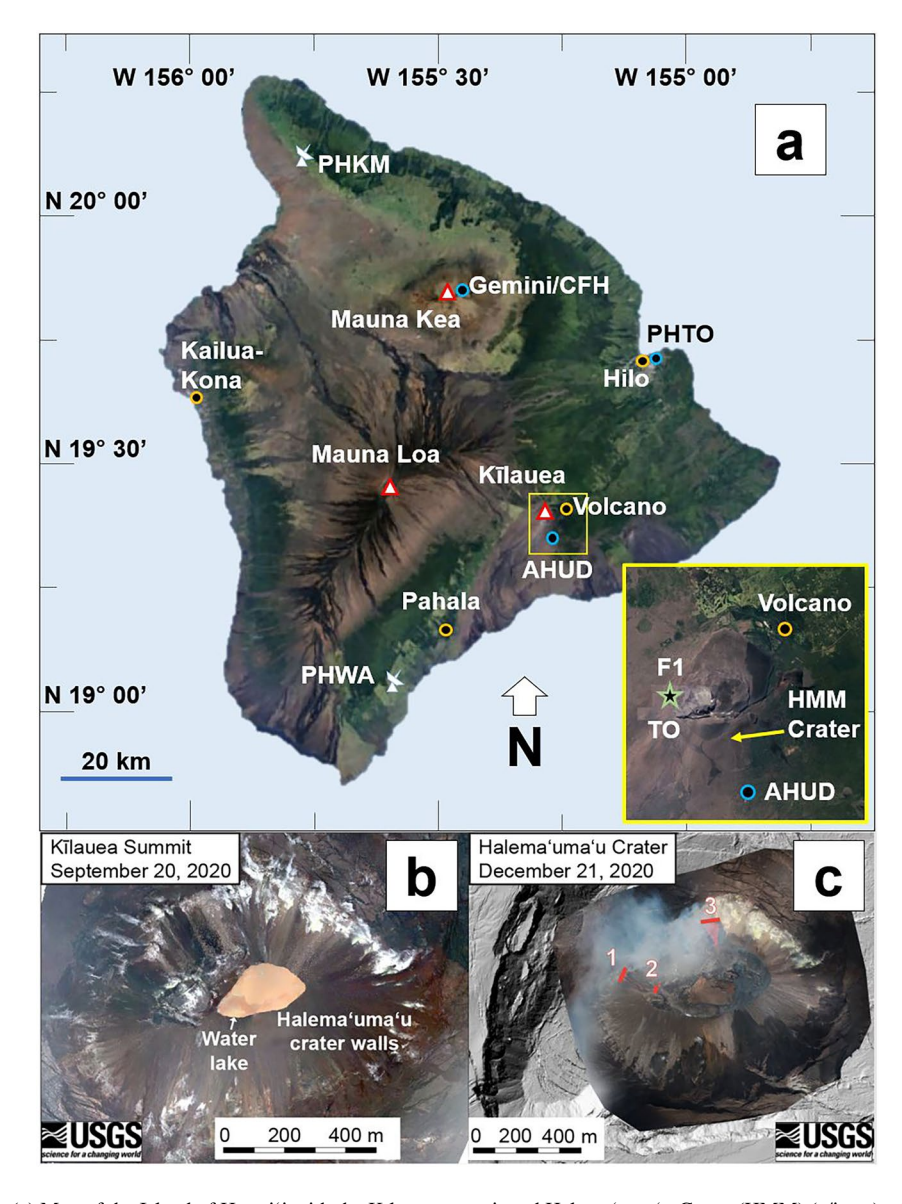


Figure 1. (a) Map of the Island of Hawai'i with the Kīlauea summit and Halema'uma'u Crater (HMM) (a/inset) with significant locations noted on the map (base layer from Google (2021)): Island of Hawai'i major volcanoes (white, red-border triangles); the South Shore (PHWA) and Kamuela-Kohala (PHKM) weather radar stations (white antenna symbols); Hawai'i population centers (yellow open circles); instrument locations (blue open circles) including the Hilo weather station (PHTO), the AHUD infrasound array, and the Gemini and Canada-France-Hawaii (CFH) Observatory cameras on Mauna Kea; the estimated location of the USGS tephra observation (green open star in inset). (b) Aerial photograph of the preeruption crater water lake taken 20 September 2020. (c) Aerial photograph of Halema'uma'u Crater lava lake from 21 December 2020, overlying a Structure-From-Motion digital elevation model (grayscale) with fissure vent locations drawn in orange bars and numbers corresponding to the west vent (1), middle vent (2), and north vent (3).

deposits, was emplaced over a 300-year period (~1500–1800 AD) when explosive hydrovolcanism was the norm (Swanson & Houghton, 2019; Swanson et al., 2012, 2014). This period includes the 1790 CE eruption that took the lives of Hawaiian warriors and their families who were caught in lethal pyroclastic density currents (Swanson et al., 2015). The growth of the summit crater water lake in 2019–2020 prompted concern that such explosive activity could return.

On 20 December 2020, an eruption in proximity to this water lake occurred, but it did not resemble the violent style of the Keanakākoʻi Tephra eruptions or any example of lava-water interaction yet documented at Kīlauea's summit. The eruption began when fissures opened in the walls of Halemaʻumaʻu Crater well above the water

CAHALAN ET AL. 2 of 23

[5252027, 2023, 3, Downloaded from

com/doi/10.1029/2022GC010718, Wiley Online Library on [16/03/2023]. See the Terms

lake surface, effusing basaltic lava that flowed into the water below (Figure 1c). The water lake boiled-off in ~90-min, sending a water-rich volcanic plume high above Kīlauea's summit and southern flank. When water from the lake was completely exhausted, the plume detached from the crater, and lava from the fissure vents fed a new lava lake in Halema'uma'u Crater.

Significant advancements have been made toward quantifying processes resulting from lava-water interactions defining the relationship between heat transfer and the onset and evolution of hydrodynamic fragmentation in these systems. The improved understanding results from laboratory experiments (Sonder et al., 2018, and many others), numerical modeling (Moitra et al., 2020; Wohletz et al., 2013), and detailed study of tephra deposits (Fitch et al., 2017; Schmith et al., 2017). These studies found that the efficacy of fragmentation is dependent on the transfer rate of thermal to kinetic energy through rapid boiling. The requisite heat transfer is dependent on the availability of hot surface area exposed by lava fragmentation initiated during mechanical mixing.

In this study, we present an analysis of multisensor data collected during the opening phase of the Kīlauea Volcano eruption to characterize the unconventional style of weakly explosive hydrovolcanism. Data from Kīlauea's dense and diverse monitoring instrumentation network (Shiro et al., 2021) provide an opportunity to model lava-water interaction and the generation of an atmospheric plume. We provide a chronological overview of the onset of the 2020 eruption (Section 2), outline the methods and data sources collected (Section 3), constrain the height evolution of the plume (Section 4), identify internal structure and composition of the plume using Doppler radar (Section 5), simulate the eruption plume with the one-dimensional (1-D) Plumeria model (Section 6), calculate heat transfer rates between lava and lake water to determine the possibility of lake boiling without lava fragmentation (Section 7), and finally, we synthesize the findings into a model for the overall eruption dynamics (Section 8).

2. Overview Chronology of the 2020–2021 Kīlauea Eruption Onset

On 20 December 2020, between 17:40 and 18:40 Hawaii Standard Time (HST = UTC-10), an earthquake swarm occurred where the upper East Rift Zone connects with summit magma reservoirs. At 18:36 HST, low-level volcanic seismic tremor began, punctuated by a sustained swarm of volcano-tectonic (VT) multiplets at the summit. At roughly 21:25 HST, the VT multiplet seismic swarm increased in intensity and at 21:29 HST the eruption began (Figure 2a) with lava effusing from a 20–30 m wide vent in the talus pile on the western wall of Halema'uma'u Crater, which is here called the west vent (Figure 1c, vent 1).

Thermal infrared cameras operated by the USGS Hawaiian Volcano Observatory (HVO) (Patrick et al., 2014, 2022) recorded lava fountaining from the west vent (Figure 1c, vent 1), cascading downslope, and reaching the water lake ~100 m below in less than 3.5 min from the eruption onset (F1 summit camera—Movie S1). It is likely that the time it took the lava to flow from the west vent to the lake was less than 3.5 min, but the summit camera's rate of image acquisition (one photo every 2 min) limited further constraint. Lava fountaining from the west vent quickly slowed to a gentle effusion after the initial eruption pulse. At 22:10 HST, the eruption transitioned back to vigorous, sustained lava fountaining, immediately followed by the opening of at least one smaller fissure to the north (Figure 1c, vent 2 or middle vent, and F1 summit camera—Movie S1) and the increase in eruptive flux coincided with an increase in sustained tremor intensity in the infrasound (Figures 2a and 2b and F1 summit camera—Movie S1). At 22:21 HST, vigorous lava fountaining from the third vent began, located along the talus pile of the crater's northern wall (Figure 1c, vent 3 or north vent, and F1 summit camera—Movie S1).

The first interaction of lava cascading into the water lake around 21:29 until 23:01 HST produced a steady plume billowing upward from the crater, which ascended slowly and drifted to the south (Figure 3 and Movies S2 and S3). The increased eruption vigor and opening of the middle and north vents (Figure 1c, vents 2, and 3, respectively) occurred contemporaneously with extensive vertical and downwind growth of the volcanic plume. During the period of peak plume height (~22:35–22:50 HST), four flashes of lightning were captured by cameras at the Canada-France-Hawaii (CFH) Observatory and the Gemini Observatory on Mauna Kea (Figure 3 and Movie S3). An HVO field crew near the Jaggar Museum witnessed lighting flashes within the plume, high above the vent at around 22:45 HST (Figure 1). Another HVO crew driving along the caldera's southwest rim (Figure 1a) noted that the road was free of any uniform blanket tephra-fall deposit from ~22:55–23:00 HST, although they did record sparse lapilli-sized clasts falling onto the roof and windshield of the vehicle. The lapilli were not collected, and their source could not be inferred during the encounter. The team also provided direct

CAHALAN ET AL. 3 of 23

1525/2027, 2023, 3, Downloaded from https://gupubs.onlinelibrary.wiley.com/doi/10.1029/2022GC010718, Wiley Online Library on [16/03/2023]. See the Terms and Conditions (https://onlinelibrary.wiley.com/ems-and-conditions) on Wiley Online Library for rules of use; OA articles are governed by the applicable Creative Commons License

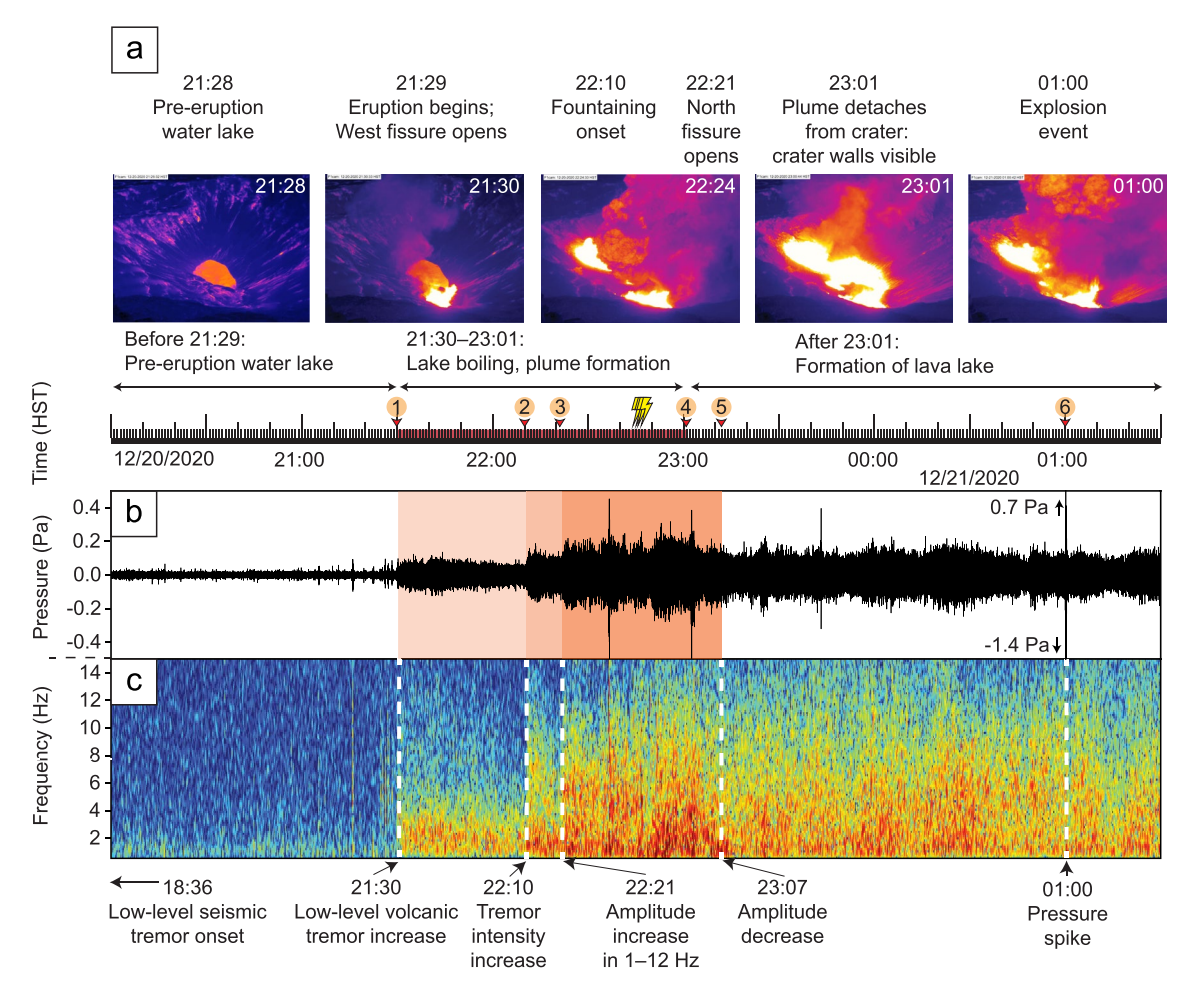


Figure 2. Chronology of the first 5.5 hr of the 20 December 2020 Kīlauea eruption from camera and infrasound observations. All times and dates are in Hawaii Standard Time (HST = UTC-10). Key events are numbered on the timeline based on (a) thermal camera (F1) images at the summit (Movie S1), (b) infrasound waveform, and (c) spectrogram from the AHUD array (lower two panels). Numbered events are as follows: (1) Eruption starts, water lake boil-off begins, and low-frequency tremor intensity increases; (2) west vent fountaining begins and tremor amplitude increases in 1–10 Hz range; (3) north vent opens and tremor amplitude increases again in 1–10 Hz range; (4) first cross-crater visual since eruption onset, lake appears "dry"; (5) infrasound 1–2 Hz amplitude decreases, remains relatively steady through 01:00 HST on 21 December 2020; (6) intralake jetting/explosion witnessed in the crater corresponds to high-amplitude infrasound spike in waveform (b), not recorded in spectrogram (c). Three smaller jetting events were recorded between 12:15 and 01:08 HST that were not detected by infrasound. The timeline highlighted in red denotes the period of water lake boil-off. Lightning flash times are indicated on the timeline by lightning bolt symbols.

visual confirmation that the water lake was gone by 23:00 HST, and that it was replaced by a rapidly growing lava lake that was comparable in size to the boiled-off water lake. By 23:01 HST, the base of the plume had detached from the crater and drifted downwind. Lava fountaining and growth of the lava lake continued steadily. Four minor gas jetting events through the lava lake surface were recorded between 12:15 and 01:08 HST. The largest of these occurred at 01:00 HST, accompanied by an audible blast recorded by the AHUD infrasound array (Figure 1b). The timeline presented in this paper concludes at 01:30 HST on 21 December 2020, after completion of the boil-off phase of the eruption.

3. Methods and Data

The abundance and variety of volcano monitoring instrumentation on the Island of Hawai'i presented an opportunity to use ground- and satellite-based measurement techniques to examine the plume that developed during the opening phase of the 20 December 2020 eruption of Kīlauea. Methods and data from an infrasound sensor array on Kīlauea's summit, a satellite infrared sensor, weather radar, and astronomical observatory webcams are presented below.

CAHALAN ET AL. 4 of 23

1525/2027, 2023, 3, Downloaded from https://agupubs.onlinelibrary.wiley.com/doi/10.1029/2022GC010718, Wiley Online Library on [16/03/2023]. See the Terms and Conditions (https://onlinelibrary.wiley.com/doi/10.1029/2022GC010718, Wiley Online Library on [16/03/2023]. See the Terms and Conditions (https://onlinelibrary.wiley.com/doi/10.1029/2022GC010718, Wiley Online Library on [16/03/2023]. See the Terms and Conditions (https://onlinelibrary.wiley.com/doi/10.1029/2022GC010718, Wiley Online Library on [16/03/2023]. See the Terms and Conditions (https://onlinelibrary.wiley.com/doi/10.1029/2022GC010718, Wiley Online Library.wiley.com/doi/10.1029/2022GC010718, Wiley Online Li

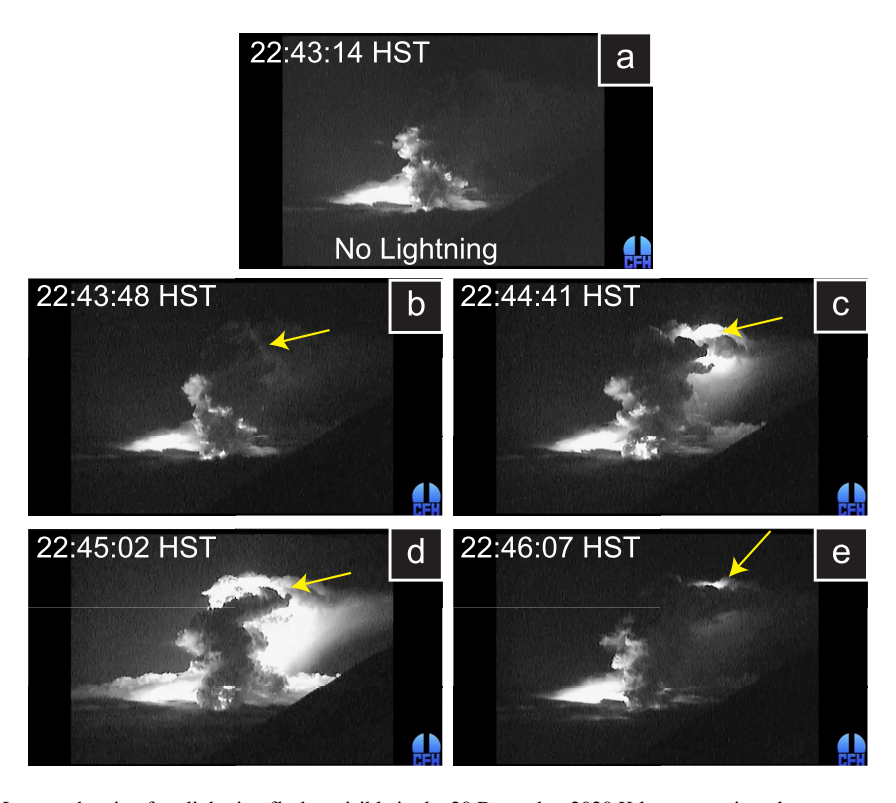


Figure 3. Images showing four lightning flashes visible in the 20 December 2020 Kīlauea eruption plume, captured by the Canada-France-Hawaii Observatory low-light webcam from the summit of Mauna Kea (location on Figure 1). Panel (a) shows a reference frame without lightning to distinguish the low-level glow from the crater. Full video in Movie S3. (b–e) Lightning flash times and locations in the plume indicated by yellow arrows.

3.1. Infrasound

The AHUD infrasound array located \sim 3.5 km south of the summit caldera (Figure 1) recorded low-intensity, low-frequency tremor (1–5 Hz band) marking the start of lava effusion and lake boiling. Lava fountaining at 22:21 HST, corresponding to the opening of the north vent (Figure 1c, vent 3), created a stronger infrasound signal in the 1–12 Hz band (Figure 2c), but there were few weak infrasound spikes (i.e., minor 'explosions') recorded during the water lake boil-off (Figures 2b and 2c). Here, we define an explosion as a rapid volume expansion of gas with vigorous energy release that would produce a detectable acoustic signal and is often accompanied by the ejection of solid fragments. Once the water lake disappeared by \sim 23:00 HST, infrasound amplitudes decreased in the 1–4 Hz frequency range. The only strong, impulsive signal (indicative of an explosion) occurred at 01:00 HST on 21 December, \sim 2 hr after the water boiled off, as a single, high-amplitude spike to 1.4 Pa (Figure 2c). This spike corresponds in time with an observed explosion near where the north vent lava flow cascading into the lava lake.

3.2. Satellite Detection of the Volcanic Plume

A widely used method of plume height determination uses satellite infrared brightness temperatures (Tupper & Wunderman, 2009; Woods & Self, 1992) to provide a measure of the thermal infrared radiation coming from the top of the cloud. For thick opaque cloud cover, it is assumed that the radiation below the cloud is absorbed in the cloud and the radiation measured represents the cloud top temperature. If the plume is tropospheric and no longer buoyant, the cloud top can be assumed to be at the same temperature as the surrounding atmosphere. NOAA's GOES-17 Advanced Baseline Imager (ABI) provides a set of multiband images of Hawai'i every 5 min at 0.5–2 km resolution (Schmit et al., 2017). We matched the coldest single-pixel brightness temperatures in the cloud from GOES-17 infrared 10.3 µm channel to corresponding heights (Figure 4, light blue circles) in the atmospheric temperature profile from the National Weather Service radiosonde from Hilo, Hawai'i, at 02:00 HST on 21 December (Figure S1 in Supporting Information S1).

CAHALAN ET AL. 5 of 23

5252027, 2023, 3, Downloaded from https://agupubs.onlinelibrary.wiley.com/doi/10.1029/2022GC010718, Wiley Online Library on [16/03/2023]. See the Terms

Figure 4. Plume height above sea level (asl) measured by radar, satellite, and webcam. Radar heights are shown in black; solid black circles give the uppermost scan detecting the plume and beam width indicated by vertical error bars; open black circles indicate the next-highest scan (next scan bottom, NSB), which provides an upper limit on the radar-derived plume height. GOES-17 satellite brightness temperature heights indicated by blue circles; Terra/MODIS height range indicated by green bar. Astrometric heights from the Gemini Observatory low-light webcam on Mauna Kea given by red dots. Note that webcam heights after 23:04 HST track the detached, downwind cloud, leading to higher values than those measured by radar and satellite directly over the vent area. Shaded regions span the time intervals used in plume rise velocity calculations (Section 3.5) using the height series from GOES-17 (blue shading) and Gemini webcam (red shading). Lightning symbol denotes the time range of lightning detection from 22:43 to 22:46 HST (Figure 3). Based on radiosonde measurements from Hilo, Hawai'i, the tropopause was ∼18 km asl and atmospheric temperatures were colder than −20°C above 7.5 km, indicated by the horizontal dashed line.

The Moderate Resolution Imaging Spectroradiometer (MODIS) instrument aboard NASA's Terra and Aqua satellites uses infrared emission and solar reflectance methods to quantify the physical and radiative properties of clouds. The cloud top height product uses a 5 km resolution algorithm to report the altitude of the cloud top (MOD06_L2, Platnick et al., 2017). The Terra satellite is on a circular sun-synchronous orbit that provides 1–2-day temporal resolution. On 20 December 2020, MODIS/Terra scanned the Hawaiian Islands at 22:47 HST, right at near-peak eruption intensity and measured the highest point of the plume at 11.2–12.0 km asl (Figure 4).

3.3. Weather Radar

The Island of Hawai'i hosts two S-band polarimetric radar units with overlapping coverage as part of the Next Generation Weather Radar (NEXRAD) multiagency project (https://www.ncdc.noaa.gov/nexradinv/). Clear weather enabled both stations to record the Kīlauea volcanic plume on 20–21 December. The South Shore station (PHWA) is 46 km from the summit of Kīlauea Volcano, yielding a higher spatial resolution than the Kamuela-Kohala Station (PHKM) at 95 km distance (locations on Figure 1a). We accessed NEXRAD level 2 data through the open-access Weather and Climate Toolkit software (Ansari et al., 2009). These data are available via commercial cloud platforms through the NOAA Open Data Dissemination (NODD) program.

Doppler radar scans may capture the plume top if the station's scanning coverage strategy covers sufficient altitude. The adaptive strategy employed by the South Shore station (PHWA) on 20 December 2020 (Figure 5) was often capped, meaning it did not capture the plume tops, due to the combination of the low angle of the uppermost scans and the proximity of the antenna to the eruptive vents. The Kamuela-Kohala station (PHKM), operated by the Federal Aviation Administration (Figure 1), was sufficiently far from the crater to capture the plume top at low-scan angles to midscan angles (above 2.8 km asl), though the added distance from antenna to target reduces the spatial resolution. Figure 4 includes NEXRAD radar-derived plume maximum heights from the South Shore station southwest of Pahala (Figure 1). We use a minimum reflectivity plume detection threshold of 18.5 dBZ, consistent with meteorological cloud top algorithms (Lakshmanan et al., 2013). In Figure 4, each data point represents a value from the center of the beam of the highest scan angle in which the plume was measured. Error bars represent the vertical beam width at the measurement location. The Next Scan Bottom (NSB in Figure 4) represents the bottom altitude of the next scan angle above the highest detection. The actual plume top value lies between the detected scan bottom and the NSB.

CAHALAN ET AL. 6 of 23

15252027, 2023, 3, Downloaded from https://agupubs.onlinelibrary.wiley.com/doi/10.1029/2022GC010718, Wiley Online Library on [1603/2023]. See the Terms and Conc

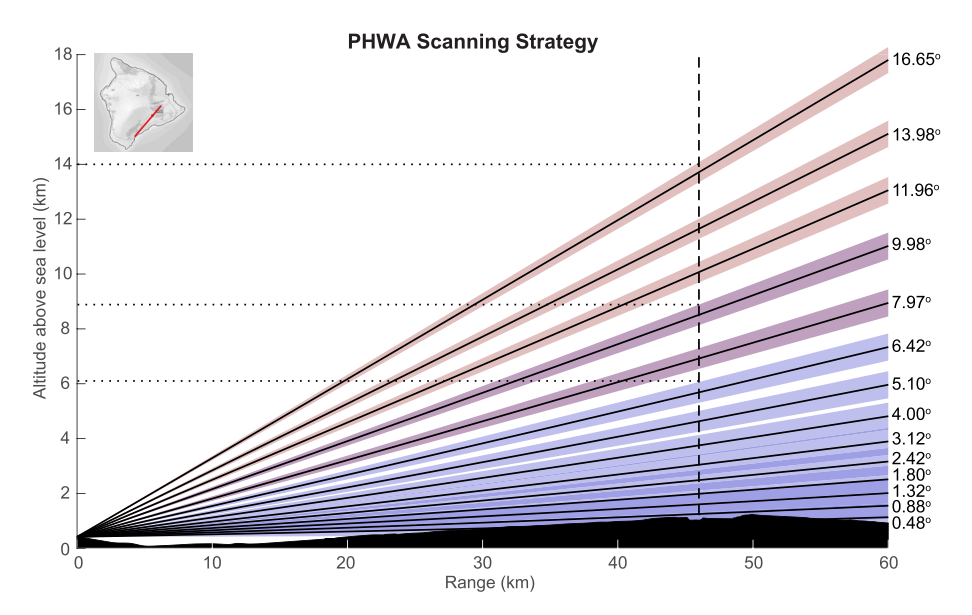


Figure 5. Adaptive radar scanning strategy for the South Shore radar station (PHWA; Figure 1). Scan elevation angles showing beam width, resolution, and overlap. Three phases of adaptive scanning were implemented: base (blue), mid (purple), and high (pink). Dashed line is the vent location. Dotted lines represent the maximum measurable altitudes for each scanning strategy. Topographic profile in the map inset along beam trace (red line) shaded in black along the lower axis.

The measure of a target's radar reflection efficiency is called reflectivity factor or reflectivity. For targets of dispersed particles such as meteorological clouds and volcanic plumes, assuming a spherical geometry and a Rayleigh scattering argument, reflectivity (*Z*) is defined as follows:

$$Z = \sum N_i D_i^6 \tag{1}$$

where N_i is the number density of particles and D_i is their diameter within the sampled volume (Marzano et al., 2013; Schneider & Hoblitt, 2013). Note the sixth power of D_i in this equation, which makes reflectivity much more sensitive to particle size than to particle concentration. Reflectivity is used to qualitatively characterize plume structure (Maki et al., 2021; Schneider & Hoblitt, 2013) and, if tephra size information is available, to estimate the mass distribution throughout the plume (Harris & Rose, 1983; Maki et al., 2021). Differential reflectivity (ZDR) is a measure of the difference in reflectivity between orthogonal axes, interpreted as a shape factor (Marzano et al., 2013). A spherical object produces a near-zero ZDR signal, an oblate object produces a positive signal, and a prolate object produces a negative one (Figure 6b). However, a rapidly rotating nonspherical object can also produce a similar signal as a spherical object. The correlation coefficient (CC) quantifies ZDR heterogeneity within a scan volume and ranges from 0 (random) to 1 (uniform) (Figure 6b). Rain clouds often return CC in excess of 0.97 since droplets can be near homogeneous in size and shape (LaRoche & Lang, 2017; Loney et al., 2002), nonuniform weather like hail or melting snow will return coefficients down to 0.7, and nonhydrometeors such as birds, insects and airplanes yield values down to 0.3. Clouds bearing volcanic particles should reflect that heterogeneity in reduced CC (Marzano et al., 2013). The combination of reflectivity, differential reflectivity, and correlation coefficient can be used to qualitatively determine the composition and structure of volcanic clouds (Figure 6c).

3.4. Webcam Data

The rise of the volcanic plume was recorded by two webcams from astronomical observatories located on Mauna Kea — the International Gemini Observatory (Gemini North) and the Canada-France-Hawaii (CFH) Telescope (Figure 1). The Gemini North cloud camera records high-pixel resolution images every 40 s that enable us to clearly identify celestial objects for astrometric determination of maximum plume heights. The low-resolution CFH camera has a higher temporal resolution suited for identifying lightning flashes in the plume. The National Science Foundation NOIRLab's Gemini Observatory (https://noirlab.edu/public/programs/gemini-observatory/) is a multinational collaborative astronomical observatory that hosts a series of cameras for monitoring sky

CAHALAN ET AL. 7 of 23

1525 2027, 2023, 3, Downloaded from https://agupubs.onlinelibrary.wiley.com/doi/10.1029/2023CGC010718, Wiley Online Library on [16/03/2023]. See the Terms and Conditions (https://onlinelibrary.wiley.com/erms-and-conditions) on Wiley Online Library for rules of use; OA articles are governed by the applicable Creative Commons Licenses and Conditions (https://onlinelibrary.wiley.com/erms-and-conditions) on Wiley Online Library for rules of use; OA articles are governed by the applicable Creative Commons Licenses and Conditions (https://onlinelibrary.wiley.com/erms-and-conditions) on Wiley Online Library for rules of use; OA articles are governed by the applicable Creative Commons Licenses and Conditions (https://onlinelibrary.wiley.com/erms-and-conditions) on Wiley Online Library for rules of use; OA articles are governed by the applicable Creative Commons Licenses and Conditions (https://onlinelibrary.wiley.com/erms-and-conditions) on Wiley Online Library for rules of use; OA articles are governed by the applicable Creative Commons Licenses and Conditions (https://onlinelibrary.wiley.com/erms-and-conditions) on Wiley Online Library for rules of use; OA articles are governed by the applicable Creative Commons Licenses and Conditions (https://onlinelibrary.wiley.com/erms-and-conditions) on Wiley Online Library for rules of use; OA articles are governed by the applicable Creative Commons Licenses and Conditions (https://onlinelibrary.wiley.com/erms-and-conditions) on Wiley Online Library for rules of use; OA articles are governed by the applicable Creative Commons Licenses and Conditions (https://onlinelibrary.wiley.com/erms-and-conditions) on Wiley Online Library for rules of use; OA articles are governed by the applicable Creative Commons (https://onlinelibrary.wiley.com/erms-and-conditions) on Wiley Online Library for rules of use; OA articles are governed by the applicable Creative Commons (https://onlinelibrary.wiley.com/erms-and-conditions) on Wiley Online Library for rules of use; OA articles are governed by

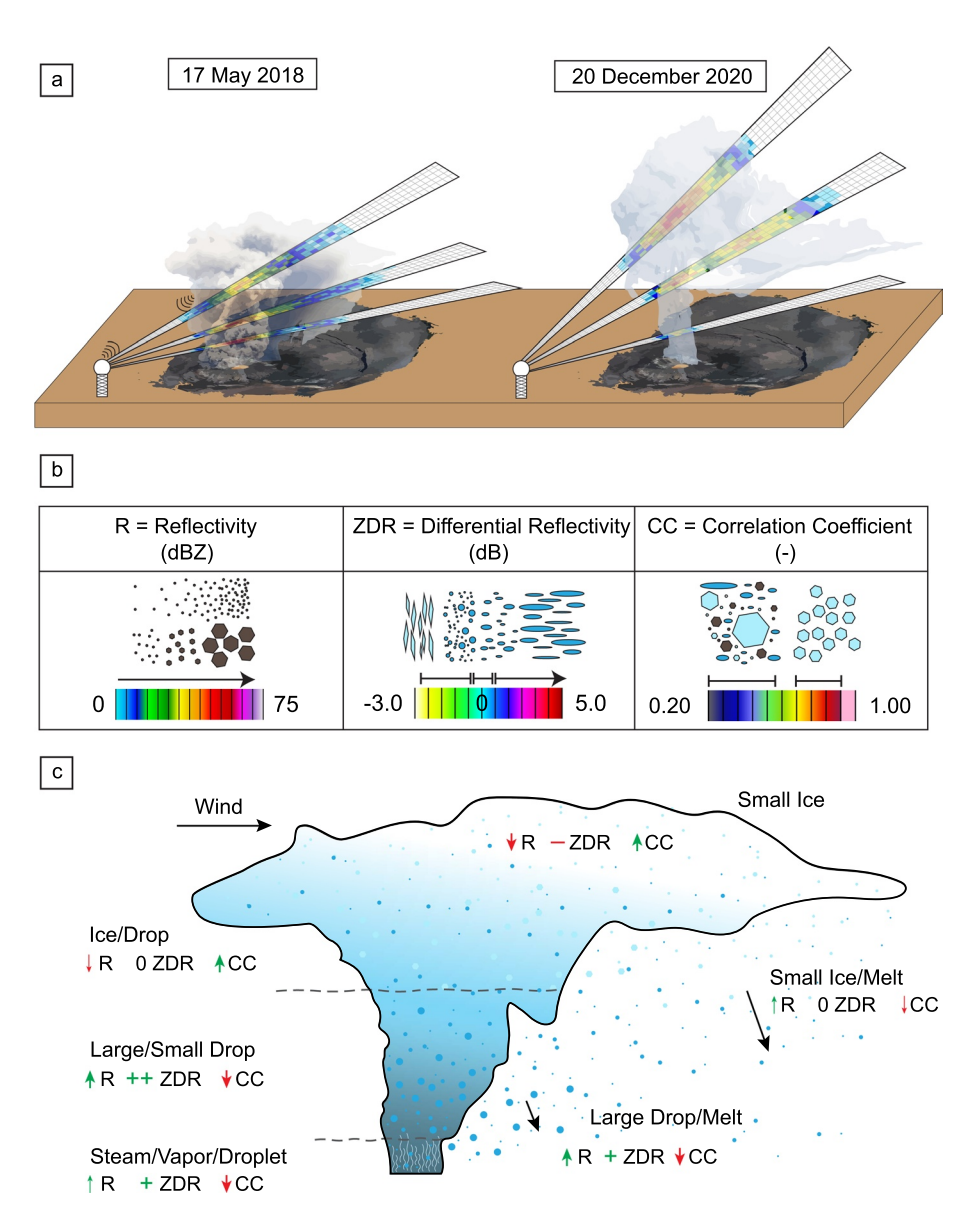


Figure 6. Illustration showing weather radar measuring reflectivity in two recent Kīlauea eruption plume types, 17 May 2018 and the 20 December 2020 plumes. (a) The 2018 plumes have the highest reflectivity near the vent, decreasing upward. The 20 December 2020 plume has the highest values well-above and downwind of the vent. (b) Relationships between measurement values and measured objects. Higher reflectivity values indicate larger particles and/or higher concentrations, Negative differential reflectivity (ZDR) indicates vertically oriented particles while near-zero values indicate spherical, and increasingly positive values suggest larger water drops. Higher correlation coefficient (CC) values quantify ZDR heterogeneity within a scan volume and range from 0 (random) to 1 (uniform), indicating higher degree of uniformity. (c) Illustration of the relationship between radar product values and a possible hydrometeor-phase composition that could produce the signal.

conditions from Mauna Kea (Figure 1). The southern horizon camera overlooks Kīlauea and captured the 20 December 2020 plume in time-lapse footage (Movie S2). A two-coordinate system astrometry method was used to determine the plume height from Gemini's southern horizon cloud camera time-lapse. Celestial objects can be located using a coordinate system that is relative to the celestial sphere of the sky, called the equatorial coordinate system. These give a static location for a celestial object. However, because of the Earth's rotation, the sky appears to move. Therefore, a horizontal coordinate system is used that captures the target's location with respect to the local horizon, reported in altitude angle and azimuth. Using the Astrometry net software (Lang et al., 2010) and a reference image taken before the eruption, we astrometrically fit the sky background and mapped the celestial coordinates for each reference pixel using built-in horizon and atmospheric distortion corrections (Lang

CAHALAN ET AL. 8 of 23

5252027, 2023, 3, Downloaded from

et al., 2010). We used the camera position to calculate the horizontal coordinates for each reference pixel. As the plume rises in the time-lapse footage, the pixel location of the plume top is chosen and compared to the reference image pixel to determine the plume-top altitude angle. With the elevation of the camera, the horizontal distance from the camera to the ground location below the identified plume top, and the plume top altitude angle, we trigonometrically determined the plume-top altitude for each time-lapse image (Figure 4, red circles). Uncertainty in these measurements associated with vertical pixel resolution and altitude angle selection are roughly 120 and 90 m, respectively.

3.5. Volcanic Lightning Detection

The two astronomical observatory webcams described in Section 3.4 also captured flashes of lightning in the volcanic plume (Figure 3). The CFH camera recorded four flashes of lightning (Figure 3 and Movie S3), providing a timestamp for each flash (between 22:43 and 22:47 HST) and a relative location within the plume (Table ST1 in Supporting Information S1). The lightning flashes noted by the HVO team near Jaggar Museum were observed within the same time window and were likely the same flashes recorded by the observatory camera. Three of these flashes were also detected by the Geostationary Lightning Mapper (GLM) aboard the GOES-17 satellite. The satellite-based GLM is an optical lightning sensor providing two-dimensional (2-D) lightning locations, flash size, and optical energy (Goodman et al., 2013). The flash at 22:46:07 HST shown in Figure 3e was not detected by GLM, but the three other flashes were located 11.5–13.0 km south of Halema'uma'u Crater (Table ST1 in Supporting Information S1). Combining the relative positions of these flashes in the webcam view (Figure 3) with their map-view locations from GLM data, and radar-derived plume height and thickness, we estimate that the flashes occurred at altitudes of 6.5–9 km asl. See Table ST1 in Supporting Information S1 for lightning characteristics.

4. Plume Height and Lightning Time Series

The plume height time series (Figure 4) reveals different phases of activity. The onset phase (21:30–22:20 HST) exhibited distinct pulses that reached ~6 km asl, observable in the Gemini webcam. During this period, the different measurement types agreed within about 0.5 km. During the peak phase (22:21–22:50 HST), the plume rose from 6 to 10–13 km asl over 20 min with the agreement between methods within 30%. The 'visible' cloud method from the Gemini webcam gave the highest values, GOES-17 brightness temperatures gave the lowest values, and radar gave intermediate heights. The single height measured by MODIS at 22:47 HST agrees with the Gemini astrometry and radar measurements at that time of ~10–12 km asl, while the GOES height is lower at ~9 km asl.

The waning phase (after 22:05 HST) shows the maximum plume height declining from its peak, which varies greatly between methods. GOES and radar data sets show gradually declining plume height until 4–5 km asl, where it stabilizes, fed by steady lava fountaining. The Gemini data show a slow decline that plateaus near 10 km asl. The disparity could result from the relative transparency of the plume and shows the dependence on the wavelength of the different observation methods. The Gemini method is based on visible observation and measures the thin yet visible plume as it tails downwind. This portion of the plume is transparent and below the selection threshold used by the other methods which capture the plume's denser region as it retreats toward the Kīlauea summit.

Plume rise velocity can be determined accurately for short intervals of steady rise (e.g., Figure 4, Gemini, 22:19–22:24 HST and 22:30–22:35 HST) or as an average over longer intervals (e.g., Figure 4, GOES-17, 22:16–22:32 HST). We determined the slope of the best fit line for each target interval to extract a rise velocity from both the Gemini webcam and GOES-17 satellite plume height series (Figure 4). Between 22:15 and 22:40 HST velocity estimates range from the minimum value of 3.3 m/s from a broad interval of GOES-17 data (22:16–22:41 HST) to the maximum value of 13.2 m/s from a ~4-min interval in the Gemini webcam series (22:30–22:34 HST). For comparison, the radar derived measurements of plume heights during most of the explosive phase of the 2009 Redoubt Volcano eruption in Alaska had a vertical velocity of ~30–60 m/s up to 10+km above the vent (Figure 10 in Schneider and Hoblitt (2013)). Comparing these observations to the time-lapse footage within the caldera (SV2) and the summit thermal cam (SV1) shows that the 22:30–22:34 HST time span captures a pulse in the plume generated immediately after opening of the north vent, whereas GOES-17 data indicate a broad increase in the maximum plume height rather than the true plume ascent velocity. Notably, the

CAHALAN ET AL. 9 of 23

5252027, 2023, 3, Downloaded from https://agupubs.onlinelibrary.wiley.com/doi/10.1029/2022GC010718, Wiley Online Library on [16/03/2023]. See the Terms and Conditions (https://onlinelibrary.wiley.com/n

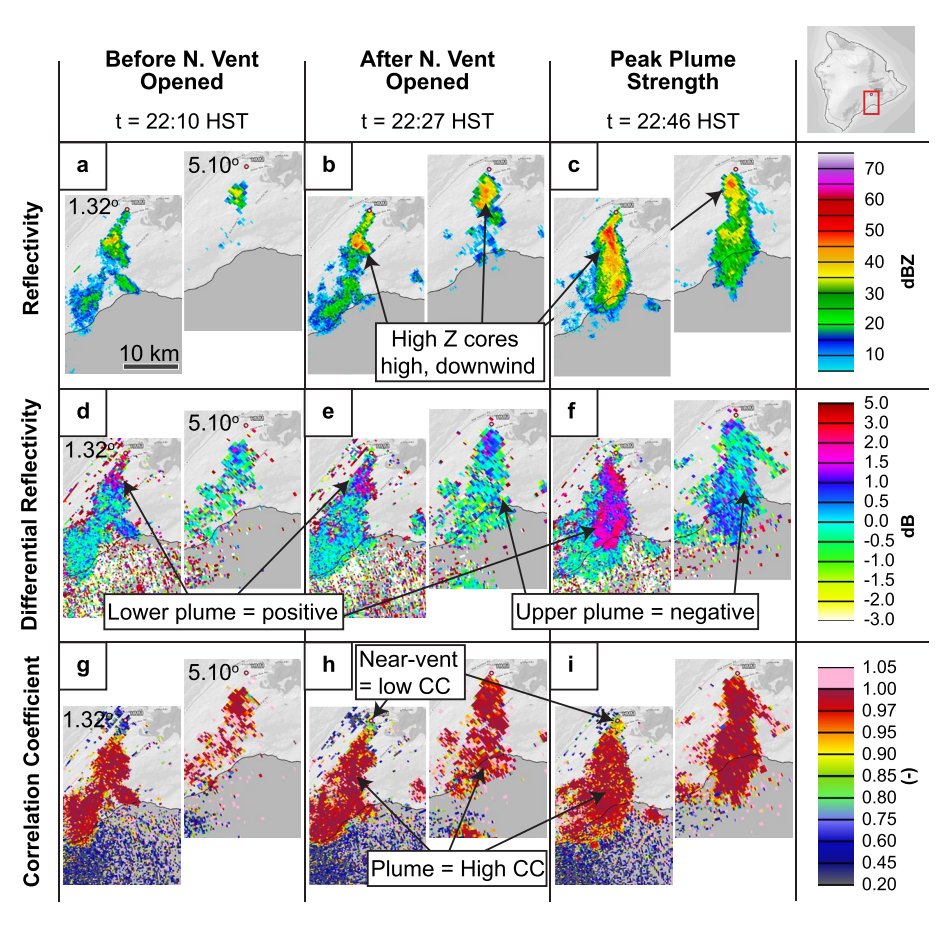


Figure 7. Radar data of the 20 December 2020 Kīlauea plume from the South Shore radar station (PHWA). Reflectivity, differential reflectivity (ZDR), and correlation coefficient (CC) data from 1.32° (low) and 5.10° (high) elevation angles at three times highlighting eruption transitions. (a–c) Reflectivity values display highly reflective cores at high altitudes in the plume and downwind from the vents. (d–f) ZDR values are high in the lower plume and near zero to negative throughout the upper plume. (g–i) CC values are small only near-caldera at low altitude, and near unity elsewhere.

GOES-17 satellite is capable of rapid scanning of specific geographic areas for volcanic cloud studies, but rapid scanning was not triggered for Hawai'i during the occurrence of this short-lived plume. The disparity in rise velocities (~4x) highlights the value in high temporal resolution data and careful selection of rise intervals when measuring and interpreting plume rise rates from remote sensing techniques.

5. Weather Radar Analysis

The earliest radar detection of the 20 December plume occurred at 21:32 HST, within 3 min of the first vent (west vent) opening. Between 21:32 and 22:23 HST, the South Shore (PHWA) station (Figure 1) showed that the plume ascend to ~5 km asl and drift slightly southeast. Reflectivity values were consistently lower near the vents (<45 dBZ) and increased to maximum values of 45–48 dBZ at 1.5–3.5 km asl and 5–9 km SSW of the summit (Figure 7 shows representative low [1.32°] and medium-high [5.10°] scan angles). In this early phase, the largest differential reflectivity (ZDR) (1.5–5 dB) was below 3.5 km asl spanning 0–8 km SSW of the vents. ZDR fell within the –2 to 0 dB range above 3.5 km asl and beyond (at most) 8 km of the vents. Near-vent correlation coefficient (CC) (<0.5 km above and within 3 km of the vents) was measured between 0.50 and 0.90. Outward from this region, CC rapidly increased, reaching 0.95–1.00.

From 22:19 to 22:51 HST, the radar recorded a rapid plume rise to 12–13 km asl and broadly increased in reflectivity to 38–58 dBZ. The largest reflectivity values of 48–58 dBZ occurred >2.5 km south of Halema'uma'u Crater. These high reflectivity cores developed around 2–4 km asl as discrete units that drifted downwind and then fell to lower altitudes, occasionally reaching ground level. Trends in ZDR followed those of the early period,

CAHALAN ET AL. 10 of 23

15252027, 2023, 3, Downloaded from https://agupubs.onlinelibrary.wiley.com/doi/10.1029/2022GC010718, Wiley Online Library on [1603/2023]. See the Terms and Conditions

and-conditions) on Wiley Online Library for rules

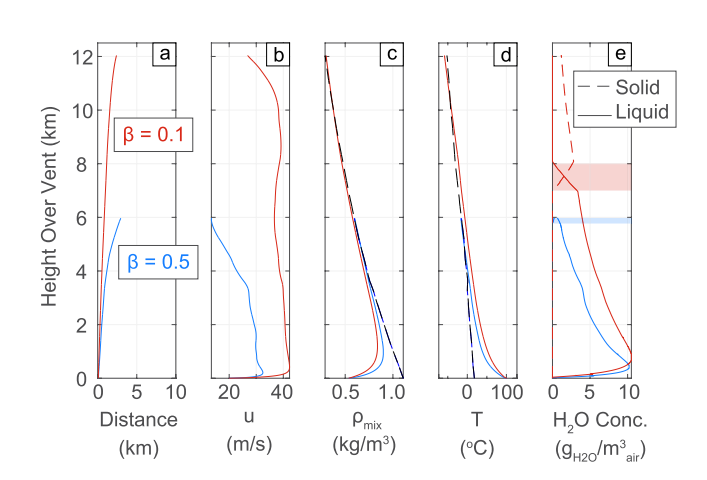


Figure 8. Vertical plume property profiles from two Plumeria runs at 22:32 HST of the 20 December 2020 Kīlauea eruption. The vertical axis starts at summit height (1.2 km asl). (Red) Initial entrainment coefficient values ($\alpha = 0.09$, $\beta = 0.5$); (Blue) Reduced crosswind entrainment ($\beta = 0.1$). (a) Horizontal distance from vent. (b) Vertical velocity profile. (c) Plume mixture density. (d) Plume temperature. (e) $\rm H_2O$ concentration highlighting phase change altitude. Note that the reduced beta (crosswind entrainment) coefficient results in doubling the projected plume height with all other parameters constant

with near-zero values near the vents, peaking in the mid plume (\sim 3.5 km asl), then shifting to negative ZDR above \sim 5 km asl. Downwind, low-altitude ZDR values measure between -1 and 1 dB. Correlation Coefficient values in this period are similar to those in the early period, with higher near-vent CC values (0.8–0.9). The high reflectivity cores consistently correspond to very high CC (0.98–1) and high ZDR values (>1.5 dB). After 22:51 HST, the plume lost strength, the top descended, and by 23:01 HST, the upper plume had detached and blown south. Reflectivity rapidly decreased near the source and steadily declined in the remaining plume until reaching radar transparency at \sim 23:50 HST.

Overall, the near-vent reflectivity values rarely exceeded \sim 44 dBZ. This differs sharply from typical explosive eruptions that have high concentrations of large particles near the vent and taper in average size fraction with distance from the vent, which produces the highest reflectivity measurements near the vent and decreases outward and upward (Marzano et al., 2013; Schneider & Hoblitt, 2013). As the plume rose to 13 km, the differential reflectivity range narrowed to -2 to 1 dB and the correlation coefficient approached 1, reflecting a transition toward homogeneity in the upper plume.

The low reflectivity, high differential reflectivity and low correlation coefficient near the vents throughout the water lake-boiling period are consistent with the interpretation of an abundance of very small particles/water droplets (low reflectivity) that are aggregating (low CC) and flatten upon rising within the plume (high ZDR) (Figure 7). Any hydrovolcanic or fountaining

lapilli or ash products in the near-vent plume would have contributed to lowering CC and raising ZDR substantially after the second and third vents opened (Figure 1c, vent 2–3). If ash or lapilli were produced, they were not entrained into the plume above 1.5 km and did not contribute to elevated reflectivity above this since the correlation coefficient values reflected near homogeneity in this region (Figure 7). Rather, as the plume rose and the dew point dropped, tiny water droplets coalesced into larger drops, and increased reflectivity to maximum values south of Halema'uma'u Crater. Drops grew to a critical size and fell from the plume shifting ZDR toward zero in the mid to upper plume (Figure 7). Small, near-spherical droplets still in suspension rose further, cooled, and began to freeze into ice crystals, as seen in the transition to negative ZDR at higher altitudes. Above this freezing altitude, the reflectivity, CC, and ZDR stabilize (Figure 7). The high crosswind velocity above 3 km generated a broad, low-altitude downwind plume component that appeared as a thin, near-zero ZDR, high-CC region. Additional quantitative investigation is needed to further strengthen the connection between radar data analysis and the dynamic processes in the plume and crater.

6. Modeling Plume Dynamics

We use Plumeria, a 1-D steady state model for convective plumes (Mastin, 2007b, 2014), to quantify the plume dynamics of the 20 December 2020 eruption and to extract a time series of water lake boiling rates from the maximum plume heights determined above. Plumeria uses a 1-D control volume analysis of mass, momentum, and energy conservation to determine the local plume properties with elevation. This tool uses two empirical entrainment parameters, α and β , which correspond to axial-flow and cross-flow entrainment. A unique consideration in eruptions of this nature is the low initial ascent velocity of the plume. Unlike other explosive eruptions that enter the atmosphere as high-velocity gas-particle jets from a confined conduit (Dufek & Bergantz, 2005; Gilbert & Sparks, 1998), the plume mass and momentum in this case are derived from unconfined, nonexplosive boiling of the summit water lake. This slow initial velocity limits the carrying capacity of the plume and likely prevents the suspension and upward transport of particles larger than fine ash. We maintain a 20 m/s initial velocity across model runs, which is the minimum velocity established in Plumeria to prevent stability issues. To conceptualize this minimum velocity value, we reflect that since rapid acceleration from the initial to peak velocity (from 20 to 30–40 m/s) occurs within ~20 m of the simulated vent height (Figure 8b), then the acceleration from 0 to 20 m/s would occur about as quickly, making the actual simulated height certainly within 100 m of the actual crater floor, and a relatively small distance relative to the plume height (Figure 8b).

CAHALAN ET AL. 11 of 23

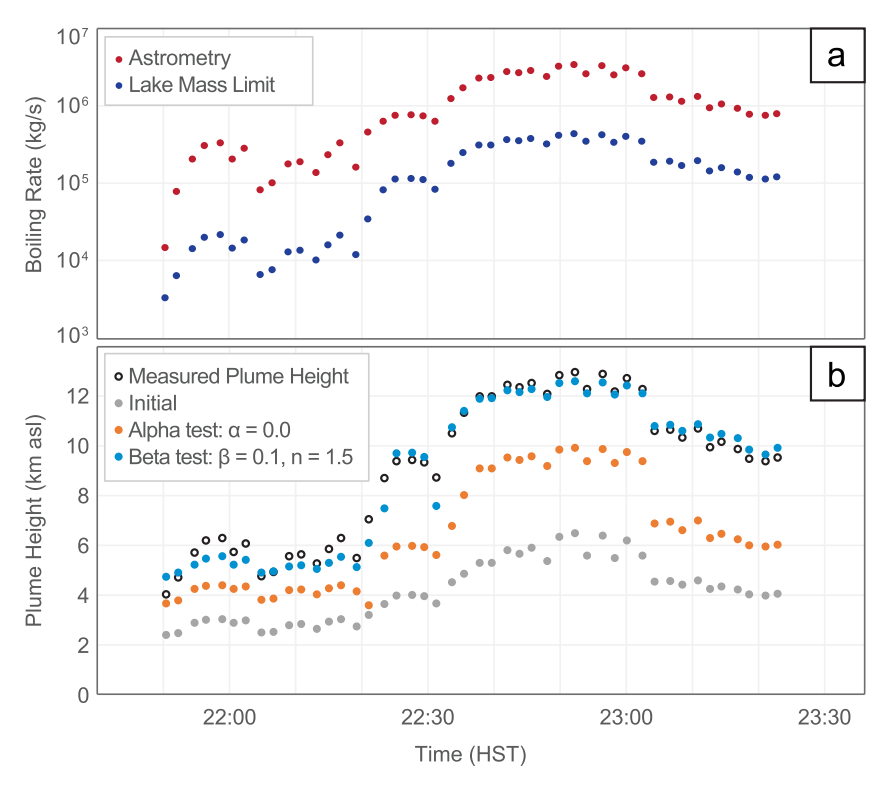


Figure 9. Boiling rates and entrainment coefficient test. (a) Boiling rates determined from Plumeria simulations reproducing the plume heights measured via the Gemini Observatory astrometry method (red). Lake-mass normalized boiling rates (blue), which are resimulated to produce the initial plume heights (gray in b). (b) Plumeria results using lake-mass normalized boiling rates and altering α (axial) and β (crosswind) entrainment coefficients from initial values of $\alpha = 0.09$, $\beta = 0.5$, n = 1.0. Simulation data are accessible in the data release by Cahalan and Mastin (2023).

The ash mass fraction in the modeled plume is set to 0.001, an arbitrarily low value that allows for model stability and that does not influence plume dynamics. The initial plume temperature is set near the water boiling temperature, consistent with thermal imagery. Small deviations in initial temperature (<40 K) were found to have no significant impact on the results. Plumeria run inputs and key outputs are available in the U. S. Geological Survey data release by Cahalan and Mastin (2023). Figure 8 shows a representative Plumeria output for the 22:32 HST plume conditions displaying five variables plotted against plume height over the vent.

A stochastic approach was taken to determine the boiling rate, where we modified steam flux into the plume by adjusting the estimated vent area, conceptually the plume base area, while holding the ascent velocity and other properties constant, until the resulting maximum plume height matches the measured plume height. The boiling rate was derived from the plume base area multiplied by the plume density and the velocity. We chose to model the astrometry plume heights that capture the visible plume top and provide a maximum end-member case, though all the plume height data sets yield thematically similar results and interpretations. The boiling rate results are shown as a time series (Figure 9a, red).

Time-integrating the results yields a total plume water mass of $\sim 1.27 \times 10^{10}$ kg, about 14 times the preeruption lake mass (Ingebritsen et al., 2021). The additional mass was unlikely to be magmatic gas: standard Kīlauea basalt possesses ~ 0.44 wt. % gas (and a typical gas composition is 0.3 wt. % H_2O , 1,110 ppm SO_2 , 265 ppm CO_2 ; Gerlach & Graeber, 1985; Lerner et al., 2021). Assuming an effusion rate between 100 and 300 m³/s with a lava density of 2,850 kg/m³, the 90-min window would release only $6.8-20.3 \times 10^6$ kg of total gas from the vents. Therefore, the erupted gas contributed negligibly to the plume dynamics relative to the total plume water mass ($\sim 10^{10}$ kg). Either an extraordinary occurrence is responsible for elevated gas eruption rates (e.g., a substantial accumulation of a gas plug in the upper magmatic network) or the modeling of this unique volcanic plume needs reevaluation.

One potential source of mismatch might be within the elusive entrainment coefficients that parameterize turbulent air entrainment in 1-D convective plume modeling (Hewett et al., 1971; Morton, 1956). Plumeria utilizes

CAHALAN ET AL. 12 of 23

5252027, 2023, 3, Downloaded from https

doi/10.1029/2022GC010718, Wiley Online Library on [16/03/2023]. See the Terms

three entrainment-related parameters, axial entrainment (α), crosswind entrainment (β), and, when applicable, an exponent (n) proposed by Devenish et al. (2010) that increases model accuracy when α and β are near equal. Suzuki and Koyaguchi (2013) presented a comparison of 1-D and 3-D plume models of the 2011 Shinmoe-dake eruption and found that 1-D models consistently overpredict crosswind entrainment in strong wind fields and suggested reducing β to 0.1–0.3 (Suzuki & Koyaguchi, 2013). McNeal et al. (2019) explored entrainment coefficient accuracy by comparing experimental and observational values and found that, even though a best-fit correlation produced entrainment coefficient values predicted many observed plume heights (α = 0.06 and β = 0.49), significant mismatches occurred for weak eruption plumes in a strong wind field. A weak plume is defined as one in which the rise velocity is less than or comparable to the wind velocity, often resulting in a distorted rise trajectory and a bent shape (Sparks et al., 1997). The 20 December 2020 Kīlauea eruption satisfied this condition—it produced a weak plume into a strong wind field.

We tested the effects of altering Plumeria entrainment coefficients to match the measured plume heights. We first established a new boiling-rate time series from the measured plume heights using buoyant plume theory (BPT) to relate plume height to boiling rate. The theory (Morton, 1956) suggests that plume height should be proportional to the fourth root of the buoyancy flux that feeds the plume. Several authors (Mastin et al., 2009; Settle, 1978; Sparks et al., 1997; Wilson et al., 1978) have shown that this proportionality roughly holds when relating the mass eruption rate of magma to plume height. For example, the Mastin et al. (2009) empirical relation between plume height (H) and MER is as follows:

$$MER_H(t) = 140H^{4.15}$$
 (2)

Our plume is driven primarily by steam rather than magma, whose heat content (\sim 2.7 MJ/kg, assuming 100% vapor at 100°C, 1 atm pressure) is somewhat greater than that of magma (\sim 1 MJ/kg, assuming specific heat of \sim 1 kJ/kg°C and a 1000°C temperature). Thus, the proportionality constant (140) in Equation 2 may differ slightly. If we ignore that difference for the moment and sum up MER_H (t) for all the time intervals illustrated by the red dots in Figure 9a, we obtain a total erupted mass of 1.27 × 10¹⁰ kg. The known mass of the lake prior to eruption was 9.16 × 10⁸ kg (Ingebritsen et al., 2021). We therefore normalize the boiling rate (MER_H) of each plume height measurement (9.16 × 10⁸/1.27 × 10¹⁰ = 7.2 × 10⁻²) (Figure 9a, blue) to isolate a source-limited boiling rate (MER_L). This adjustment ensures that the new plume height-time profile maintains the same relative shape for a minimum end-member not involving gas from the vent nor potential suspended ash mass.

We ran Plumeria with the source-limited boiling rates at various entrainment coefficient combinations and compared the plume height profiles. We found that large changes in axial entrainment coefficient, α , yielded minor changes in plume height (Figure 9b, orange). However, the simulations were highly sensitive to changes in crosswind entrainment, β . When modified to $\beta = 0.1$ (from $\beta = 0.5$) and the Devenish exponent to n = 1.5 (from n = 1.0), simulated plume heights were consistently within 500 m and always within 2 km of the observation (Figure 9b light blue). Modifying the crosswind coefficient to a value (0.1) near the axial entrainment coefficient (0.06) has been shown to be more accurate when modified by a Devenish exponent of n = 1.5 (Devenish, 2013; Devenish et al., 2010). The greatest mismatch occurred in the early plume phase prior to the second and third vent openings. This likely represents a period where the boiling rate was low enough that the plume was influenced by vent-derived gasses, so simulated plumes that do not account for these processes are consistently lower. We find β reduction critical to accurate 1-D plume simulation under the influence of strong winds, which was 75–100 m/s at upper plume altitudes during this eruption (Figure S1 in Supporting Information S1).

7. Calculating Heat Transfer Rates During Lava-Water Interaction

Lava-water contact does not necessitate explosive ash generation, exemplified by various occurrences of lava ocean-entry along the Hawaiian coastline (Edmonds & Gerlach, 2006; Mattox & Mangan, 1997; Moore et al., 1973; Soule et al., 2021). Ocean entry sites typically produce explosions immediately following the collapse of an active lava shelf, when hot lava can extrude directly from fractured lava tubes into onrushing ocean waves (Mattox & Mangan, 1997). The wave action drives coarse-scale lava-water mixing, necessary for increasing the lava-water interfacial area and initiating steam explosion-driven fragmentation (Zimanowski et al., 1997). Unlike the ocean-entry environment, the 2020 preeruption Kīlauea water lake did not have waves to force mixing along the water's edge and would have required a self-generated turbulent mixing mechanism.

CAHALAN ET AL. 13 of 23

15252027, 2023, 3, Downloaded from https://agupubs.onlinelibrary.wiley.com/doi/10.1029/2022GC010718, Wiley Online Library on [16/03/2023]. See the Terms

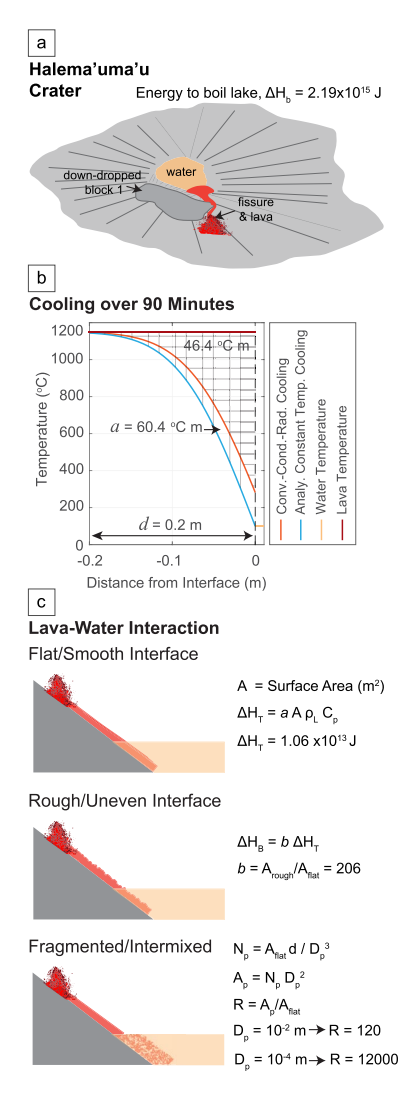


Figure 10. Heat flow modeling schematic showing Halema'uma'u Crater (a), results of numerical and analytical models with cooling curves integrated to find the cooling coefficient *a* (b), and relationships between lava-water interface geometries and heat transfer rates (c).

Several lines of evidence suggest that the first interaction of lava-water during the boiling event was nonexplosive. AHUD infrasound data captured a signal from water lake boiling that was low frequency and much lower in amplitude than the 01:00 HST explosion. Lyons et al. (2019) found that infrasound signals from explosions in the 2016–2017 Bogoslof volcano submarine eruptions were consistently attenuated at higher frequencies when water was present. While the scale and geometry of water interaction in the Bogoslof and Kīlauea volcanic eruptions were different—Bogoslof volcano having a submerged vent—we cannot rule out the possibility of signal attenuation at least contributing to the weakened, low frequency-dominated boil-off signal. The AHUD infrasound data cannot solely rule out the occurrence of explosions during lake boiling.

The absence of detectable ash in the plume and no ash fallout near-crater area indicate that mechanisms of posteruptive ash generation, such as glassy rind shedding (Mastin, 2007a), were not significant. Glassy rinds form as a thin skin on rapidly cooling lava in both air and water. The rind is often shed by mechanical processes due to the coupling of the brittle rind and deformable molten interior. Turbulent mixing along the lava-water lake interface would have generated ash from rind-shedding to be lofted in the plume.

The production of fine material via lava-water interaction would greatly enhance the rate of water lake boiling. With simple heat transfer modeling, we determined if nonviolent boiling could yield sufficient heat transfer rates to have boiled off the 2020 water lake in 90 min. Given the 9.16×10^5 m³ lake volume, we calculated an average boiling rate of 1.70×10^5 kg/s. Further, since we know the approximate lake water temperature prior to eruption (~70°C) from the F1 thermal cam, and can simplify the water chemistry by assuming pure water with a heat capacity ($c_{p,w}$) of 4,180 J/kgK, density (ρ_w) of 1,000 kg/m³, and latent heat of vaporization (L_V) of 2.26 × 10⁶ J/kg (e.g., Haar, 1984), we calculate the minimum energy required to heat and boil the lake (ΔE):

$$\Delta E = \rho_w V_w (c_{p,w} \Delta T_w + L_V) \tag{3}$$

By dividing ΔE (2.19 × 10¹⁵ J) by the boiling time (90 min) and the lava-water interfacial area (for now we simplify as the water lake surface area, 5.4 × 10⁴ m²), we calculate an average heat flux of ~7.05 MW/m² needed to boil the lake within the 90-min window.

The average heat flux is a baseline with which we can test multiple processes of lava-water interaction to determine their role in the boil-off event (Figure 10).

First, we evaluate the most straightforward case of heat exchange between an intact, flat lava flow and a water lake. We used 1-D heat transfer calculations modeled after Mastin (2007a) to quantify the heat transfer, assuming a flat, tabular, and static lava body with infinite thickness that immediately contacts water and begins cooling through a single contact surface (Figure 10a). We numerically solve conduction in the lava body with convective and radiative heat loss at the lava-water interface parameterized with a hydrodynamic regime-dependent heat transfer coefficient (Kreith & Bohn, 1986). The second calculation considers a fast heat transfer end-member that assumes a constant temperature boundary condition (Cronenberg, 1980). The temperature within the lava body is calculated using an analytical error function formulation from Carslaw and Jaeger (1959). Heat flux at the surface is calculated from the instantaneous thermal gradient and thermal conductivity.

We used estimates for the starting lava temperature of 1200° C, water temperature of 70° C, and the thermal properties listed above, including the specific heat capacity of water at 4,180 J/kgK, the density of water at 1,000 kg/m³, the latent heat of vaporization of water at 2.26×10^6 J/kg, the specific heat capacity of basalt at 1,300 J/kgK, and a temperature-dependent heat transfer coefficient for pool boiling, a boiling mechanism/regime for a hot body in contact with water (Kreith & Bohn, 1986, Figure 8.1). With this, we produce the lava edge

CAHALAN ET AL. 14 of 23

15252027, 2023, 3, Downloaded from https

thermal profiles in Figure 10b for heat loss after 90 min. Integrating between the resulting and initial temperature curves yields a timescale-dependent cooling coefficient, a, from a thermal skin depth, d, which we can use to calculate heat loss for different lava surface areas.

In Figure 10c, we show three surface area-heat transfer relationships with an accompanying calculation. For the modeled flat, tabular lava flow with a generous area equal to the lake surface, 5.4×10^4 m², using the analytical approach from above and an estimated lava density of 2,500 kg/m³ and specific heat of 1,300 J/kgK, we find the total heat transferred in 90 min to be 1.06×10^{13} J. Comparing this heat loss to the energy required to heat and boil the lake $(2.19 \times 10^{15} \, \text{J})$, the heat transfer rate is ~206x less than is necessary to boil the water lake in 90 min. This disparity could be accounted for by increasing the surface area available for heat loss by either adding a more realistic surface texture to the lava flow or by fragmenting the lava flow into particles through lava-water interaction induced break-up (Figure 10c). To test these options, we calculated the surface area increase factor, R, generated by breaking the outer lava flow, of thickness equivalent to the thermal skin depth, d, in Figure 10b, into cubic particles of size D_p . This latter parameter is conceptualized as a characteristic texture length scale, either as fragmented particles or as surface roughness. Two values for D_p and R are given in Figure 10c. Characteristic length values between 10 µm and 2 mm produce R values that far exceed the required increase in the surface area (600-60,000x compared to 206x). Conversely, the length scale needed to achieve the required surface area increase is ~6 mm. Particles of this size are not typical of fine hydromagmatic fragmentation (Walker & Croasdale, 1971; Wohletz, 1983) and too large to loft in a plume with a near-zero initial rise velocity. We conclude that by considering the lava surface texture in the millimeter to decimeter scale, the previously modeled flat lava case would yield sufficiently high heat transfer rates to generate the observed activity without generating fine lava fragmentation. In short, neither ash generation nor explosive lava breakup is necessary to generate this plume.

We suspect that this eruption need not have been this docile. If lava fountains had erupted directly into the water lake, turbulent mixing could have instigated rapid heat transfer and fragmentation that would have produced a much more violent event. Detailed field studies of past phreatomagmatic eruptions at Kīlauea and elsewhere, as well as a comprehensive modeling investigation of eruptions involving crater lakes, are needed to better assess the complex hazards associated with these eruptions.

8. Discussion

8.1. Synthesis of Eruption Dynamics

The 20 December 2020 eruption began with potential for explosive lava-water mixing but evolved to a mostly nonhazardous eruption. Within 90 min of the start of the eruption, the lava had boiled the entirety of the water lake and produced a plume that reached a maximum height between 11 and 13 km asl. Aggregated multisensor data sets and direct observations suggest an absence of explosions from water-lava interaction in the crater. Water lake boiling and plume formation may have generated a weak infrasound signal in the 1-5 Hz frequencies that decreased around 23:07 HST (Figure 1), though it certainly did not produce explosions or impulsive infrasound signals near the scale of explosions observed at 01:00 HST. The lack of acoustic "explosions" during lava-water interaction at the start of the eruption suggests that the boiling process was, at most, weakly explosive due to low rates of heat transfer from lava to water from insufficient mixing along the lava-water interface. Changes to the lava-water entry condition that could have led to a more explosive outcome include eruption directly into the water lake or nearer the lake margin, resulting in an initial lava-lake interface geometry that promotes mixing or water entrapment. Plume formation occurred directly from lake boiling with likely minor contributions from vent-derived magmatic gases. The lack of a jet thrust component at the base of the weakly explosive lake boiling plume implies that the plume would have started rising with minimal momentum. Despite this, the low tephra concentration plus heated steam from lake boiling produced an initial positive buoyancy that drove rapid upward acceleration. As the water-rich, ash-poor plume rose, the dominant hydrous phase changed from water vapor near the vent to water droplets in low to mid altitudes, and ice in the upper plume altitudes. Any ash transported in the plume would have contributed to seeding the ice-nuclei. At least four lighting flashes occurred at altitudes corresponding to water and ice coexistence; flashes were witnessed from the ground and detected via satellite. As part of the plume fell to lower altitudes downwind, transported ice melted and precipitated to the ground, as suggested by radar analysis. This 'rain' fell from the plume in the uninhabited terrain kilometers south of the crater rim drive and could possibly have carried and deposited suspended ash beyond regions sampled for tephra. While the nature and amount of ash produced in the plume remain unstudied, we know from field observations

CAHALAN ET AL. 15 of 23

5252027, 2023, 3, Downloaded from https://agupubs.onlinelibrary.wiley.com/doi/10.1029/2022GC010718, Wiley Online Library on [16/03/2023]. See the Terms

that no ash fell on the southwestern caldera rim drive immediately following the start of lake boil-off and that tephra-fall began on the road immediately after the north wall vent opened. As water lake-boiling diminished, the plume detached from the crater and drifted downwind. At 01:00 HST on 21 December, hours after the lake had clearly dried, an explosion from the lava lake was recorded by the AHUD infrasound array as the highest amplitude signal of the eruption. The strength of this signal and the absence of similar high-amplitude pulses during boiling of the water lake provide an upper constraint on "explosivity" during that period.

8.2. Origin of Volcanic Lightning

It can be challenging to distinguish the roles of various charging mechanisms in volcanic plume electrification (Cimarelli & Genareau, 2022; Méndez Harper & Dufek, 2016; Van Eaton et al., 2016). Near-vent lighting predominantly occurs by silicate charging mechanisms (Cimarelli et al., 2022), while hydrometeor charging in the liquid water-ice coexistence zone is thought to trigger globally detectable lightning in the upper plume (Van Eaton et al., 2020, 2022). The four lightning flashes detected by webcam during this eruption (three of which were also detected by the satellite-based Geostationary Lightning Mapper, GLM) occurred after the opening of the north vent around 22:25 HST. The flashes were located 11.5–13 km south of the crater (Table ST1 in Supporting Information S1) at heights of 6.5–9 km asl, estimated by cross referencing GLM locations with radar detections of the top and bottom of the plume. Radar observations indicated ice nucleation between 6.5 and 8 km asl based on the shift from positive to negative differential reflectivity, which indicates a transition from liquid to frozen water drops (Figure 6). The GLM locations occur within this freezing zone (Table ST1 in Supporting Information S1). Additionally, our 1-D plume modeling suggests ice formation at heights of 7–8 km asl, lending further support that detectable volcanic lightning occurred primarily in the ice-producing region of the plume.

Van Eaton et al. (2020, 2022) and Prata et al. (2020) characterized previous hydromagmatic eruptions as water-rich and ash-depleted and determined that vigorous up-drafts and rapid ice formation drove subsequent lightning-rich volcanic thunderstorms. Although the four lightning flashes detected in this Kīlauea plume are modest in comparison to other lightning-rich eruptions, our findings are consistent with electrification by ice-forming mechanisms. This example provides an end-member case of lightning activity in a plume containing minimal volcanic ash. Additionally, this is the first time that volcanic lightning has been simultaneously captured by ground-based video and satellite-GLM, making it a rich case study for future work.

8.3. Inferring Eruption Rate From Plume Dynamics

The 11–13 km height of this plume exceeds estimates of all other Kīlauea plumes in historical times with possible exceptions in 1790 CE (12–15 km asl estimated in Swanson et al., 2015), and the ~12 km asl Kulanaokuaiki 3 Tephra plume (>1 ka), one of the most explosive Kīlauea eruptions in the past ~2.5 kyr (Fiske et al., 2019). For comparison, the 2018 Kīlauea summit collapse event plumes ranged from 2.4 to 4.1 km asl, apart from the ~9 km asl 17 May 2018 plume, as measured from the South Shore (PHWA) NEXRAD radar. The height of this plume is comparable to eruptions with sizes of VEI 3–4, such as from Crater Peak vent (Mount Spurr, Alaska) in 1992 (McGimsey et al., 2001) and Hekla volcano (Iceland) in 1970 (Thorarinsson & Sigvaldason, 1972). Empirical height-rate relationships (e.g., Mastin et al., 2009, Equation 1; Sparks et al., 1997, Equation 5.1) suggest that an eruption with a plume height 12 km above vent level would have a mass eruption rate of millions of kilograms per second. Over a 1.5-hr period, this translates into a few tens of millions of cubic meters of tephra, placing it in the middle of the VEI 3 range in terms of erupted volume.

We know from field evidence that this eruption was not close to VEI 3. Eyewitness accounts near the southern caldera rim reported ash-free surfaces 10 min before the detachment of the boil-off plume. We used the Ash3d dispersion model (Schwaiger et al., 2012) to simulate tephra transport from a plume having roughly the average height and duration as this one, with the wind field present at the time of the eruption (Appendix A). Using an eruption rate calculated from the empirical height-rate curve (Mastin et al., 2009, Equation 1), we find (Figure A1) that the tephra thickness near Kīlauea's summit and south flank would be a few millimeters to a centimeter or so. Prehistoric VEI 3 summit eruptions such as the Keanakāko'i 1790 CE are still thicker at the summit, decimeters or so (Swanson et al., 2015; Swanson & Houghton, 2019). The area covered extends south and southwest along Highway 11 and includes Pahala and Nā'ālehu, congruent with past explosions (e.g., 1924 CE Kīlauea summit eruptions; Stearns, 1925).

CAHALAN ET AL. 16 of 23

15252027, 2023, 3, Downloaded from

and Cond

Using Mastin et al. (2009, Equation 1), the two-sigma standard error in the eruption rate for a given plume height is roughly an order of magnitude. The fact that no deposit or resuspension problems were noted southwest or south (downwind) of the summit suggests that the erupted volume was at least an order of magnitude less than predicted. The lack of evidence of ash in the plume indicates that ash production was less than might be anticipated by models constrained by maximum plume height. However, there is insufficient evidence to suggest that the plume was ash free. A 3-D radar reproduction of the plume (Movie S4) emphasizes that the critical areas for deposition from the plume would not have been near the caldera, but around 3 km south of the caldera rim. Field observers were not in this area and may have missed this hypothetical deposit.

One reason for the large discrepancy in the eruption rate inferred from plume height and from geological constraints based on deposit volume stems from the eruption style. In most explosive eruptions, the fragmented magma and exsolved gases, whose heat drives the plume upward, rise within the column. In the December 2020 Kīlauea plume, however, the magma transferred its heat to water but did not rise with it. The added heat, without the added mass load, drove the plume to a greater maximum height than what modeling predicts given the constrained source mass. This may be a common height-boosting mechanism in some explosive magma-water interactions that causes the plumes of some water-driven eruptions to rise to greater heights than expected given the mass eruption rate of tephra.

Another possible reason for this discrepancy is the influence of regional atmospheric conditions on upward plume mobility. The tropopause altitude above Hawai'i is significantly higher than at Crater Peak vent (Mount Spurr, Alaska) and Hekla volcano (Iceland), which are in the sub-Arctic. Upward plume mobility in the atmosphere would be mostly similar in the sub-Arctic and tropics up to the elevation of the tropopause, above which only hot plumes will continue into the stratosphere. The lower altitude sub-Arctic tropopause would limit the vertical reach of the plume.

8.4. Opportunities for Future Studies and Improved Volcano and Eruption Monitoring

This study and the remaining questions suggest possible improvements in monitoring future eruptions at Kīlauea and other volcanoes. Detection of volcanic lightning during this eruption demonstrates that even ash-poor plumes can become electrified and create lightning discharges that are detectable by satellites. This finding suggests that in situ electrical monitoring at Kīlauea's summit would be valuable for detecting and characterizing a range of eruptive processes, including the generation of ash-poor plumes. Real-time, openly available Doppler radar products can be compiled into standard response operations, for example, by generating maps of radar reflectivity to help constrain forecasts of ashfall, augmenting information from the application of Ash3D. Additionally, the value of the Doppler radar for studying volcanic eruptions can be expanded through the development of radar data processing tools specific to volcano eruption applications, similar to the many data products widely available for weather and precipitation analysis and forecasting. Routine simulations of ash plume dynamics using codes such as Ash3d (Schwaiger et al., 2012) that incorporate real-time weather parameters (wind patterns) for hypothetical Kīlauea eruptions can be incorporated into response plans that project the expected spatial distribution of ashfall. Continuous processing and automation of astrometry data collected by the Gemini Observatory on Mauna Kea (Figure 1) would be helpful for quantifying plume heights. The development and deployment of an automated ash sampling array (Marchetti et al., 2022; Shimano et al., 2013) could provide a continuous record of tephra fall. Time-constrained tephra records would inform ongoing ash dispersal modeling, provide context for radar and satellite analysis and yield a valuable tephra-sample data set for petrology and ash morphology analyses.

9. Conclusions

On 20 December 2020, at 21:29 Hawaii Standard Time (HST), a fissure opened, sending lava flowing into a confined water lake at the bottom of Halema'uma'u Crater near the summit of Kīlauea Volcano. Based on analyses of diverse data sets presented in this study, we find that:

1. The water lake completely disappeared 90 min after the onset of the eruption, as evidenced by the summit thermal camera imagery. Calculations of heat transfer between the lava flow and the lake water suggest that the heat flux required to boil the lake in 90 min is possible without fine-scale lava fragmentation. Lava-water interaction had to have occurred with minimal coarse-scale mixing that could have initiated hydromagmatic fragmentation.

CAHALAN ET AL. 17 of 23

15252027, 2023, 3, Downloaded from https

Wiley Online Library on [16/03/2023]. See the Terms

nelibrary.wiley.com/terms-and-conditions) on Wiley Online Library for rules of use; OA articles are governed by the applicable Creative Commons Licens

- 2. Boiling of the water lake in the Halema'uma'u Crater produced a low-energy, low-amplitude acoustic signal recorded by infrasound sensors on the summit of Kīlauea. The lack of a strong impulsive acoustic signal indicates that lava-water interaction did not produce significant steam explosions.
- 3. Lava-water interaction generated an ash-poor plume that rose 10–13 km above sea level at measured ascent velocities ranging between 3 and 13 m/s, as indicated by radar, satellite, and visual camera observations. The calculated plume heights from these different methods are within ±30%.
- 4. Ash was not visually observed on the ground downwind of the eruption immediately following the cessation of lake-boiling. USGS Ash3d dispersion simulations of a theoretical Volcanic Explosivity Index (VEI) three eruption plume, one that might be anticipated from the 20 December plume height alone, suggested that a 1–10 mm-thick-tephra deposit should have formed southwest of the caldera. However, no tephra deposit was observed.
- 5. We used one-dimensional modeling of the volcanic plume with the USGS Plumeria code incorporating widely used values ($\alpha = 0.09$, $\beta = 0.5$) for air entrainment. These simulations underestimate the maximum measured plume height, indicating that the crosswind entrainment parameter must be reduced to accurately simulate this slowly ascending plume in a strong wind field.
- 6. Four lightning flashes detected by webcam (three of which were also detected by satellite) occurred about 1 hr after the onset of the volcanic eruption. Based on radar data, we estimate that these flashes formed when the volcanic plume began nucleating ice at elevations of 6.5–8 km above sea level. One-dimensional plume modeling results predict a freezing altitude between 7 and 8 km asl, consistent with our observation of volcanic lightning in the ice-producing region of the plume.

Appendix A

In order to estimate the thickness of tephra that might fall during this event, we used a web interface of the Ash3d tephra transport model (Schwaiger et al., 2012) (https://vsc-ash.wr.usgs.gov). This model interface uses a wind field for the time and date of this eruption from the NOAA/NCEP Reanalysis 1 meteorological model (Kalnay et al., 1996). Volcanological inputs to the model are given in Tables A1, A2, and A3. We use a time-varying plume height given in Table A2 with erupted volumes during each time segment calculated from plume height using the empirical height-rate relationship of Mastin et al. (2009, Equation 1) (Figure A1).

	Table A1 Inputs and Model Settings Used for Ash3d Tephra Simulation		
	Parameter	Value(s)	
Ī	Eruption start time	20 December 2020 21:20 HST	
	Duration	1 hr	
	Vent location	155.284°W, 19.406°N	
	Horizontal resolution	0.03° latitude and longitude	
	Vertical resolution	1 km	
	Model domain	158–154°W, 17–20°N, 0–13 km asl	
	Diffusivity	$0 \text{ m}^2\text{/s}$	
	<i>Note.</i> The eruption start time and duration were assigned based on the approximate time period when the plume rose about		

Note. The eruption start time and duration were assigned based on the approximate time period when the plume rose above about 7 km.

CAHALAN ET AL. 18 of 23

15252027, 2023, 3, Downloaded from https://agupubs.onlinelibrary.wiley.com/doi/10.1029/2022GC010718, Wiley Online Library on [16/03/2023]. See the Terms and Conditions (https://onlinelibrary.wiley.com/ems-and-conditions) on Wiley Online Library for rules of use; OA articles are governed by the applicable Creative Commons Licenses

Time (HST) on 20 December 2020	H_asl (km)	H_avl (km)	MER (kg/s)	V (km ³ DRE)
21:20–21:30	8	6.7	3.77×10^{5}	9.05×10^{-5}
21:30–21:40	10	8.7	1.11×10^{6}	2.68×10^{-4}
21:40–21:50	10	8.7	1.11×10^{6}	2.68×10^{-4}
21:50–22:00	10	8.7	1.11×10^{6}	2.68×10^{-4}
22:00–22:10	9	7.7	6.72×10^{5}	1.61×10^{-4}
22:10-22:20	7	5.7	1.93×10^{5}	4.63×10^{-5}

Note. The terms H_asl and H_avl refer to the plume height above sea level and above vent level, respectively. The vent elevation above sea level for these simulations was taken to be 1.3 km. The term MER refers to the mass eruption rate of solid particles in kg/s, and V refers to the total volume of solids, in cubic kilometers of dense-rock equivalent (DRE). To convert from erupted mass to volume DRE, we assume a magma density of 2,500 kg/m³.

 Table A3

 Grain-Size Distribution Used for Ash3d Simulation

Diam (mm)	Mass fraction	Density (kg/m³)	Shape factor F
2.00	0.061	800	0.44
1.00	0.071	1,040	0.44
0.50	0.227	1,280	0.44
0.250	0.219	1,520	0.44
0.177	0.054	1,640	0.44
0.125	0.044	1,760	0.44
0.088	0.028	1,880	0.44
0.218	0.018	600	1
0.203	0.072	600	1
0.190	0.120	600	1
0.177	0.072	600	1
0.165	0.018	600	1

Note. Fall velocities in Ash3d are calculated using Wilson and Huang (1979), which approximates particles as ellipsoids with semimajor, intermediate, and semiminor axes of a, b, and c, respectively. The shape factor F (right-hand column) is defined as F(b+c)/2a and is used in the fall-velocity calculation. Size distribution is as given below. We used a grain-size distribution in which 30% of the tephra is fine ash, similar to the 2009 Redoubt event 5 eruption (Mastin et al., 2013). The fine ash is represented in this table as aggregates (in italics). The remainder consists of particles 0.125-2 mm in diameter that fall individually, with densities that range linearly with $\log_2(\text{diam})$ from 800 kg/m³ for the largest clasts to 1,880 kg/m³ for the smallest. This too is based on a grain-size distribution inferred for the 2009 Redoubt event 5 (Mastin et al., 2013).

CAHALAN ET AL. 19 of 23

5252027, 2023, 3, Downloaded from https://agupubs.onlinelibrary.wiley.com/doi/10.1029/2022GC010718, Wiley Online Library on [16/03/2023]. See the Terms

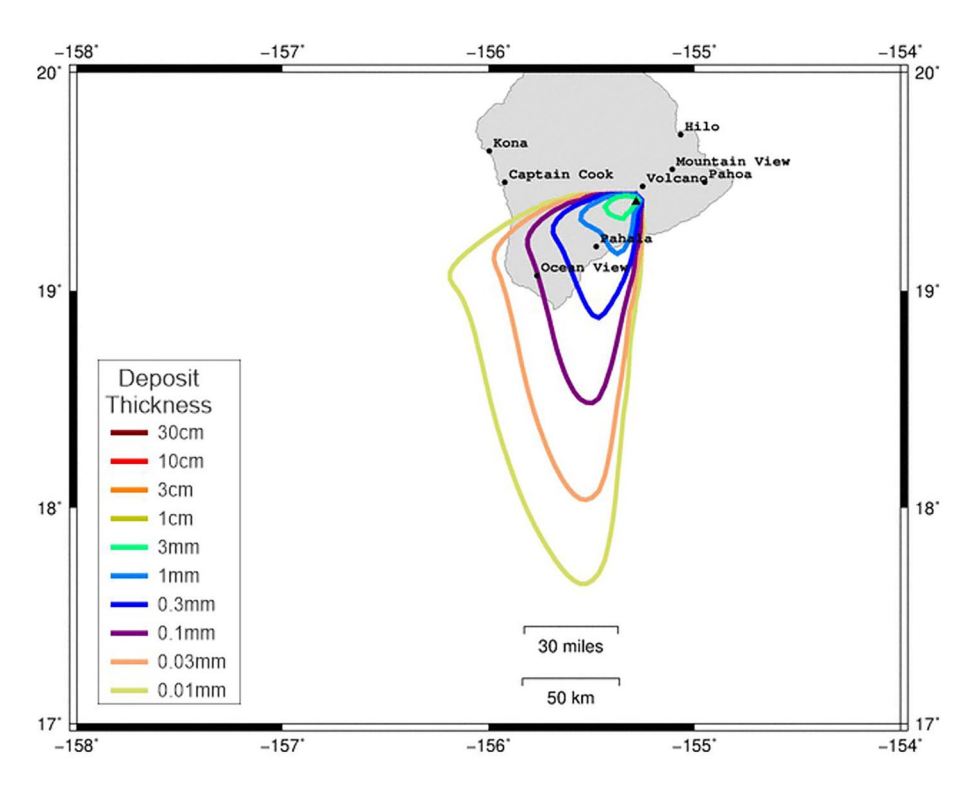


Figure A1. Isopach map of deposit thickness calculated from the Ash3d model simulation.

Conflict of Interest

The authors declare no conflicts of interest relevant to this study.

Data Availability Statement

NEXRAD radar data are available online at NOAA's National Centers for Environmental Information NEXRAD archive (https://www.ncdc.noaa.gov/nexradinv/displaygraphs.jsp?mm=12&dd=21&yyyy=2020& product=AAL2&filter=&id=PHWA). GOES-17 satellite data, including Geostationary Lightning Mapper data, are available through the University of Wisconsin-Madison Space Science and Engineering Center (SSEC) Satellite Data Services (SDS) repository (https://inventory.ssec.wisc.edu/inventory/#search&start_ time:2020-12-21%2008:00;end_time:2020-12-21%2012:00;satellite:GOES-17;type:ABI;coverage:FD). mal IR data from the Kīlauea summit are available in the U.S. Geological Survey data release by Patrick et al. (2022) (https://doi.org/10.5066/P9HQHDMH). MODIS data from the Terra and Aqua satellites are available at NASA's Level-1 and Atmosphere Archive and Distribution System Distributed Active Archive Center (DAAC) (https://ladsweb.modaps.eosdis.nasa.gov/about/) and easily viewable via the online EOSDIS Worldapplication (https://worldview.earthdata.nasa.gov/?v=-156.36764758479868,18.58744382732024,-153.7589947595545,19.82909481492023&l=MODIS_Terra_Cloud_Top_Height_Night,Reference_ Labels_15m(hidden),Reference_Features_15m(hidden),Coastlines_15m&lg=true&t=2020-12-21-T17%25% 21Z). Infrasound data are available as part of the National Science Foundation's Incorporated Research Institutions for Seismology (IRIS) archive (https://www.iris.edu/hq/). This data can be requested at https://ds.iris. edu/ds/nodes/dmc/forms/bregfast-request/, using the search criteria for the AHUD array (https://ds.iris.edu/ mda/HV/AHUD/?starttime=2011-04-06&endtime=2599-12-31). Atmospheric sounding data are available via the University of Wyoming's Weather Web (https://weather.uwyo.edu/upperair/sounding.html). The version of the U.S. Geological Survey's Plumeria code used in this study can be accessed online (https://theghub.org/ resources/1197). All Plumeria inputs and important outputs used in this study are available in the U. S. Geological Survey data release by Cahalan and Mastin (2023) (https://doi.org/10.5066/P9V4I3MM).

CAHALAN ET AL. 20 of 23

15252027, 2023, 3, Downloaded from https://agupubs

Acknowledgments

This research utilized data sets from a wide variety of instruments maintained by scientists and staff at the USGS Hawaiian Volcano Observatory (HVO), National Science Foundation's NOIRlab's Gemini Observatory, and the Canada-France-Hawaii Telescope Observatory. The HVO geophysics group's response efforts enabled the analysis of early seismicity. Ashton Flinders and Jefferson Chang provided helpful insight into the eruption seismic data. This work benefited greatly from discussions with Don Swanson and Jim Kauahikaua, both of whom have contributed decades of research to understanding the history and workings of Hawaiian volcanoes. This work was supported by the Additional Supplemental Appropriations for Disaster Relief Act of 2019 (P.L. 116-20) following the eruption of Kīlauea Volcano in 2018. We thank David Schneider, Greg Valentine, and an anonymous reviewer for their constructive comments. Any use of trade, firm. or product names is for descriptive purposes only and does not imply endorsement by the U.S. Government. The USGS authors are funded by the U.S. Geological Survey Volcano Hazards Program.

References

- Ansari, S., Hutchins, C., Del Greco, S., Stroumentova, N., & Phillips, M. (2009). The weather and climatetoolkit. In 25th Conference on Interactive Information and Processing Systems (IIPS) for Meteorology, Oceanography, and Hydrology (Vol. 6A, p. 4). Phoenix, AZ, American Meteorological Society. Retrieved from https://ams.confex.com/ams/89annual/techprogram/paper_146485.htm
- Cahalan,, R. C., & Mastin,, L. G. (2023). Plumeria simulations of 20 December 2020 Ktlauea Volcano eruption plume. U.S. Geological Survey Data Release. https://doi.org/10.5066/P9V4I3MM
- Carslaw,, H. S., & Jaeger,, J. C. (1959). Conduction of heat in solids (2nd ed., p. 510). Clarendon.
- Cimarelli,, C., Behnke,, S., Genareau,, K., Méndez Harper,, J., & Van Eaton,, A. R. (2022). Volcanic electrification: Recent advances and future perspectives. *Bulletin of Volcanology*, 84(8), 78. https://doi.org/10.1007/s00445-022-01591-3
- Cimarelli,, C., & Genareau,, K. (2022). A review of volcanic electrification of the atmosphere and volcanic lightning. *Journal of Volcanology and Geothermal Research*, 422, 107449. https://doi.org/10.1016/j.jvolgeores.2021.107449
- Cronenberg., A. W. (1980). Recent developments in the understanding of energetic molten fuel-coolant interactions. *Nuclear Safety*, 21(3), 319–337.
- Devenish,, B. J. (2013). Using simple plume models to refine the source mass flux of volcanic eruptions according to atmospheric conditions. Journal of Volcanology and Geothermal Research, 256, 118–127. https://doi.org/10.1016/J.JVOLGEORES.2013.02.015
- Devenish,, B. J., Rooney,, G. G., Webster,, H. N., & Thomson,, D. J. (2010). The entrainment rate for buoyant plumes in a crossflow. Boundary-Layer Meteorology, 134(3), 411–439. https://doi.org/10.1007/S10546-009-9464-5
- Dufek,, J., & Bergantz,, G. W. (2005). Transient two-dimensional dynamics in the upper conduit of a rhyolitic eruption: A comparison of closure models for the granular stress. *Journal of Volcanology and Geothermal Research*, 143(1–3), 113–132. https://doi.org/10.1016/j.ivolgeores.2004.09.013
- Edmonds,, M., & Gerlach,, T. M. (2006). The airborne lava-seawater interaction plume at Kilauea Volcano, Hawai'i. Earth and Planetary Science Letters, 244(1–2), 83–96. https://doi.org/10.1016/J.EPSL.2006.02.005
- Fiske,, R. S., Rose,, T. R., Swanson,, D. A., Andrews,, B. J., & Nichols,, A. R. (2019). The Kulanaokuaiki-3 tephra, 900 CE: Products of a remarkably energetic pyroclastic eruption at Kīlauea Volcano, Hawai'i, USA. GSA Bulletin, 131(9–10), 1537–1554. https://doi.org/10.1130/b35063.1
- Fitch,, E. P., Fagents,, S. A., Thordarson,, T., & Hamilton,, C. W. (2017). Fragmentation mechanisms associated with explosive lava-water interactions in a lacustrine environment. *Bulletin of Volcanology*, 79(12), 1–16. https://doi.org/10.1007/s00445-016-1087-3
- Gerlach,, T. M., & Graeber,, E. J. (1985). Volatile budget of Kilauea volcano. Nature, 313(6000), 273–277. https://doi.org/10.1038/313273a0
 Gilbert,, J. S., & Sparks,, R. S. J. (1998). The physics of explosive volcanic eruptions. Geological Society Special Publication (Vol. 145). Geological Society
- Goodman, S. J., Blakeslee, R. J., Koshak, W. J., Mach, D., Bailey, J., Buechler, D., et al. (2013). The GOES-R geostationary lightning mapper (GLM). Atmospheric Research. 125–126, 34–49. https://doi.org/10.1016/j.atmosres.2013.01.006
- Google. (2021). Island of Hawai'i. Retrieved from https://earth.google.com/web
- Haar,, L. (1984). NBS/NRC steam tables. CRC Press.
- Harris,, D. M., & Rose,, W. I. (1983). Estimating particle sizes, concentrations, and total mass of ash in volcanic clouds using weather radar. Journal of Geophysical Research, 88(C15), 10969–10983. https://doi.org/10.1029/JC088iC15p10969
- Hewett,, T. A., Fay,, J. A., & Hoult,, D. P. (1971). Laboratory experiments of smokestack plumes in a stable atmosphere. Atmospheric Environment, 5(9), 767–789. https://doi.org/10.1016/0004-6981(71)90028-X
- Ingebritsen,, S. E., Flinders,, A. F., Kauahikaua,, J. P., & Hsieh,, P. A. (2021). Modeling groundwater inflow to the new crater lake at Kīlauea Volcano, Hawai'i. *Groundwater*, 59(1), 7–15. https://doi.org/10.1111/gwat.13023
- Kalnay, E., Kanamitsu, M., Kistler, R., Collins, W., Deaven, D., Gandin, L., et al. (1996). The NCEP/NCAR 40-year reanalysis project. Bulletin of the American Meteorological Society, 77(3), 437–471. https://doi.org/10.1175/1520-0477(1996)077<0437:TNYRP>2.0.CO;2
- Kreith,, F., & Bohn,, M. S. (1986). *Principles of heat transfer* (p. 700). Harper Collins.
- Lakshmanan, V., Hondl., K., Potvin, C. K., & Preignitz, D. (2013). An improved method for estimating radar echo-top height. Weather and Forecasting, 28(2), 481–488. https://doi.org/10.1175/WAF-D-12-00084.1
- Lang,, D., Hogg,, D. W., Mierle,, K., Blanton, M., & Roweis,, S. (2010). Astrometry.net: Blind astrometric calibration of arbitrary astronomical images. The Astronomical Journal, 139(5), 1782–1800. https://doi.org/10.1088/0004-6256/139/5/1782
- LaRoche,, K. T., & Lang,, T. J. (2017). Observations of ash, ice, and lightning within pyrocumulus clouds using polarimetric NEXRAD radars and the national lightning detection network. *Monthly Weather Review*, 145(12), 4899–4910. https://doi.org/10.1175/MWR-D-17-0253.1
- Lerner,, A. H., Wallace,, P. J., Shea,, T., Mourey,, A. J., Kelly,, P. J., Nadeau,, P. A., et al. (2021). The petrologic and degassing behavior of sulfur and other magmatic volatiles from the 2018 eruption of Kīlauea, Hawai'i: Melt concentrations, magma storage depths, and magma recycling. Bulletin of Volcanology, 83(43), 43. https://doi.org/10.1007/s00445-021-01459-y
- Loney,, M. L., Zrnić,, D. S., Straka,, J. M., & Ryzhkov,, A. V. (2002). Enhanced polarimetric radar signatures above the melting level in a supercell storm. *Journal of Applied Meteorology*, 41(12), 1179–1194. https://doi.org/10.1175/1520-0450(2002)041<1179:eprsat>2.0.co;2
- Lyons,, J. L., Haney,, M. M., Fee,, D., Wech,, A. G., & Waythomas,, C. F. (2019). Infrasound from giant bubbles during explosive submarine eruptions. *Nature Geoscience*, 12(11), 952–958. https://doi.org/10.1038/s41561-019-0461-0
- Maki,, M., Kim,, Y., Kobori,, T., Hirano,, K., Lee,, D., & Iguchi,, M. (2021). Analyses of three-dimensional weather radar data from volcanic eruption clouds. *Journal of Volcanology and Geothermal Research*, 412, 107178. https://doi.org/10.1016/j.jvolgeores.2021.107178
- Marchetti,, E., Poggi,, P., Delle Donne,, D., Pistolesi,, M., Bonadonna,, C., Bagheri,, G., et al. (2022). Real-time tephra-fallout accumulation rates and grain-size distributions using ASHER (ASH collector and sizER) disdrometers. *Journal of Volcanology and Geothermal Research*, 429, 107611. https://doi.org/10.1016/j.jvolgeores.2022.107611
- Marzano,, F., Picciotti,, E., Montopoli,, M., & Vulpiani,, G. (2013). Inside volcanic clouds: Remote sensing of ash plumes using microwave weather radars. *Bulletin of the American Meteorological Society*, 94(10), 1567–1586. https://doi.org/10.1175/BAMS-D-11-00160.1
- Mastin,, L. G. (1997). Evidence for water influx from a caldera lake during the explosive hydromagmatic eruption of 1790, Kilauea volcano, Hawaii. *Journal of Geophysical Research*, 102(B9), 20093–20109. https://doi.org/10.1029/97jb01426
- Mastin,, L. G. (2007a). Generation of fine hydromagmatic ash by growth and disintegration of glassy rinds. *Journal of Geophysical Research*, 112(B2), B02203. https://doi.org/10.1029/2005JB003883
- Mastin,, L. G. (2007b). A user-friendly one-dimensional model for wet volcanic plumes. Geochemistry, Geophysics, Geosystems, 8(3), Q03014. https://doi.org/10.1029/2006GC001455
- Mastin,, L. G. (2014). Testing the accuracy of a 1-D volcanic plume model in estimating mass eruption rate. *Journal of Geophysical Research:* Atmospheres, 119(5), 2474–2495. https://doi.org/10.1002/2013JD020604

CAHALAN ET AL. 21 of 23

5252027, 2023, 3, Downloaded from https

- Mastin, L. G., Christiansen, R. L., Thornber, C., Lowenstern, J., & Beeson, M. (2004). What makes hydromagmatic eruptions violent? Some insights from the Keanakako'i ash, Kilauea Volcano, Hawai'i. *Journal of Volcanology and Geothermal Research*, 137(1–3), 15–31. https://doi.org/10.1016/j.jvolgeores.2004.05.015
- Mastin,, L. G., Guffanti,, M., Servranckx,, R., Webley,, P. W., Barsotti,, S., Dean,, K. G., et al. (2009). A multidisciplinary effort to assign realistic source parameters to models of volcanic ash-cloud transport and dispersion during eruptions. *Journal of Volcanology and Geothermal Research*, 186(1–2), 10–21, https://doi.org/10.1016/j.jvolgeores.2009.01.008
- Mastin, L. G., Schwaiger, H., Schneider, D. J., Wallace, K. L., Schaefer, J., & Denlinger, R. P. (2013). Injection, transport, and deposition of tephra during event 5 at Redoubt Volcano, 23 March, 2009. *Journal of Volcanology and Geothermal Research*, 259, 201–213. https://doi.org/10.1016/j.jvolgeores.2012.04.025
- Mattox,, T. N., & Mangan,, M. T. (1997). Littoral hydrovolcanic explosions: A case study of lava-seawater interaction at Kilauea Volcano. *Journal of Volcanology and Geothermal Research*, 75(1–2), 1–17. https://doi.org/10.1016/S0377-0273(96)00048-0
- McGimsey, R. G., Neal., C. A., & Riley., C. (2001). Areal distribution, thickness, volume, and grain size of tephra-fall deposits from the 1992 eruptions of Crater Peak vent, Mt. Spurr Volcano, Alaska. U.S. Geological Survey Open-File Report 01-0370 (p. 38). U.S. Government Printing Office. https://doi.org/10.3133/ofr01370
- McNeal,, J. S., Freedland,, G., Mastin,, L. G., Cal,, R. B., & Solovitz,, S. A. (2019). Investigating the accuracy of one-dimensional volcanic plume models using laboratory experiments and field data. *Journal of Geophysical Research: Solid Earth*, 124(11), 11290–11304. https://doi.org/10.1029/2018IB017224
- Méndez Harper,, J., & Dufek,, J. (2016). The effects of dynamics on the triboelectrification of volcanic ash. *Journal of Geophysical Research*, 121(14), 8209–8228. https://doi.org/10.1002/2015jd024275
- Moitra, P., Sonder, I., & Valentine, G. (2020). The role of external water on rapid cooling and fragmentation of magma. Earth and Planetary Science Letters, 537(1), 116194. https://doi.org/10.1016/j.epsl.2020.116194
- Moore, J. G., Phillips,, R. L., Grigg,, R. W., Peterson,, D. W., & Swanson,, D. A. (1973). Flow of lava into the sea, 1969–1971, Kilauea Volcano, Hawaii. Geological Society of America Bulletin, 84(2), 537–546. https://doi.org/10.1130/0016-7606(1973)84<537:FOLITS>2.0.CO;2
- Morton,, B. R. (1956). Turbulent gravitational convection from maintained and instantaneous sources. *Proceedings of the Royal Society of London, Series A, Mathematical and Physical Sciences*, 234(1196), 1–23, https://doi.org/10.1098/rspa.1956.0011
- Nadeau,, P. A., Diefenbach,, A. K., Hurwitz,, S., & Swanson,, D. A. (2020). From lava to water: A new era at Kīlauea. Eos, Earth and Space
- Science News, 101. https://doi.org/10.1029/2020E0149557
 Patrick,, M. R., Orr., T., Antolik,, L., Lee,, L., & Kamibayashi,, K. (2014). Continuous monitoring of Hawaiian volcanoes with thermal cameras.
- Journal of Applied Volcanology, 3(1), 1. https://doi.org/10.1186/2191-5040-3-1
 Patrick,, M. R., Younger,, E. F., & Tollett,, W. (2022). Thermal camera data for the summit of Kīlauea Volcano, 2019–2022. U.S. Geological
- Survey Data Release. https://doi.org/10.5066/P9HQHDMH
- Platnick,, S., Ackerman,, S., King,, M., Menzel,, P., Frey,, R., & Wind,, G. (2017). MODIS atmosphere L2 cloud product (06_L2). NASA MODIS Adaptive Processing System, Goddard Space Flight Center.
 Prata,, A. T., Folch,, A., Prata,, A. J., Biondi,, R., Brenot,, H., Cimarelli,, C., et al. (2020). Anak Krakatau triggers volcanic freezer in the upper
- troposphere. Scientific Reports, 10(3584), 3584. https://doi.org/10.1038/s41598-020-60465-w
- Schmit,, T. J., Griffith,, P., Gunshor,, M. M., Daniels,, J. M., Goodman,, S. J., & Lebair,, W. J. (2017). A closer look at the ABI on the GOES-R series. Bulletin of the American Meteorological Society, 98(4), 681–698. https://doi.org/10.1175/BAMS-D-15-00230.1
- Schmith, J., Höskuldsson, Á., & Holm, P. M. (2017). Grain shape of basaltic ash populations: Implications for fragmentation. Bulletin of Volcanology, 79, 14. https://doi.org/10.1007/s00445-016-1093-5
- Schneider,, D. J., & Hoblitt,, R. P. (2013). Doppler weather radar observations of the 2009 eruption of Redoubt Volcano, Alaska. *Journal of Volcanology and Geothermal Research*, 259, 133–144. https://doi.org/10.1016/j.jvolgeores.2012.11.004
- Schwaiger,, H., Denlinger,, R., & Mastin,, L. G. (2012). Ash3d: A finite-volume, conservative numerical model for ash transport and tephra deposition. *Journal of Geophysical Research*, 117(B4), B04204. https://doi.org/10.1029/2011JB008968
- Settle., M. (1978). Volcanic eruption clouds and the thermal power output of explosive eruptions. *Journal of Volcanology and Geothermal Research*, 3(3–4), 309–324. https://doi.org/10.1016/0377-0273(78)90041-0
- Shimano,, T., Nishimura,, T., Chiga,, N., Shibasaki,, Y., Iguchi,, M., Miki,, D., & Yokoo,, A. (2013). Development of an automatic volcanic ash sampling apparatus for active volcanoes. *Bulletin of Volcanology*, 75(12), 1–7. https://doi.org/10.1007/s00445-013-0773-7
- Shiro,, B. R., Zoeller,, M. H., Kamibayashi,, K., Johanson,, I. A., Parcheta,, C., Patrick,, M. R., et al. (2021). Monitoring network changes during the 2018 Kīlauea Volcano Eruption. Seismological Research Letters, 92(1), 102–118. https://doi.org/10.1785/0220200284
- Sonder,, I., Harp., A., Graettinger,, A. H., Moitra, P., Valentine,, G. A., Büttner,, R., & Zimanowski,, B. (2018). Meter-scale experiments on magma-water interaction. *Journal of Geophysical Research: Solid Earth*, 123(12), 10597–10615. https://doi.org/10.1029/2018JB015682
- Soule,, S. A., Zoeller,, M., & Parcheta,, C. (2021). Submarine lava deltas of the 2018 eruption of Kīlauea volcano. *Bulletin of Volcanology*, 83(4), 1–16. https://doi.org/10.1007/S00445-020-01424-1/FIGURES/10
- Sparks,, R. S. J., Bursik,, M. I., Carey,, S. N., Gilbert,, J. S., Glaze,, L. S., Sigurdsson,, H., & Woods,, A. W. (1997). Volcanic plumes (p. 574). John Wiley & Sons.
- Stearns,, H. T. (1925). The explosive phase of Kilauea Volcano, Hawaii, in 1924. Bulletin of Volcanology, 2, 193–208. https://doi.org/10.1007/
- Suzuki, Y. J., & Koyaguchi, T. (2013). 3D numerical simulation of volcanic eruption clouds during the 2011 Shinmoe-dake eruptions. Earth, Planets and Space, 65(10), 581–589. https://doi.org/10.5047/eps.2013.03.009
- Swanson, D. A., & Houghton, B. F. (2019). Products, processes, and implications of Keanakāko'i volcanism, Kīlauea Volcano, Hawai'i. In M. P. Poland, M. O. Garcia, V. E. Camp, & A. Grunder (Eds.), Field volcanology: A tribute to the distinguished career of Don Swanson (Vol. 238, pp. 159–190). Geological Society of America Special Papers.
- Swanson,, D. A., Rose,, T. R., Fiske,, R. S., & McGeehin,, J. P. (2012). Keanakāko'i Tephra produced by 300 years of explosive eruptions following collapse of Kīlauea's caldera in about 1500 CE. *Journal of Volcanology and Geothermal Research*, 215–216, 8–25. https://doi.org/10.1016/j.jvolgeores.2011.11.009
- Swanson,, D. A., Rose,, T. R., Mucek,, A. E., Garcia, M. O., Fiske,, R. S., & Mastin,, L. G. (2014). Cycles of explosive and effusive eruptions at Kīlauea Volcano, Hawai'i, *Geology*, 42(7), 631–634. https://doi.org/10.1130/G35701.1
- Swanson,, D. A., Weaver,, S. J., & Houghton,, B. F. (2015). Reconstructing the deadly eruptive events of 1790 CE at Kīlauea Volcano, Hawai'i. Geological Society of America Bulletin, 127(3–4), 503–515. https://doi.org/10.1130/B31116.1
- Thorarinsson,, S., & Sigvaldason,, G. (1972). The Hekla eruption of 1970. Bulletin of Volcanology, 36(2), 269–288. https://doi.org/10.1007/BF02596870

CAHALAN ET AL. 22 of 23

15252027, 2023, 3, Downloaded from https://agupubs

wiley.com/doi/10.1029/2022GC010718, Wiley Online Library on [16/03/2023]. See the Terms and Conditions (https://onlinelibrary.wiley.com/terms.

and-conditions) on Wiley Online Library for rules

of use; OA articles are governed by the applicable Creative Commons

- Tupper,, A., & Wunderman,, R. (2009). Reducing discrepancies in ground and satellite-observed eruption heights. *Journal of Volcanology and Geothermal Research*, 186(1–2), 22–31. https://doi.org/10.1016/j.jvolgeores.2009.02.015
- Van Eaton,, A. R., Amigo,, Á., Bertin,, D., Mastin,, L. G., Giacosa,, R. E., González,, J., et al. (2016). Volcanic lightning and plume behavior reveal evolving hazards during the April 2015 eruption of Calbuco volcano, Chile. Geophysical Research Letters, 43(7), 3563–3571. https://doi.org/10.1002/2016GL068076
- Van Eaton,, A. R., Schneider,, D. J., Smith,, C. M., Haney,, M. W., Lyons,, J. J., Said., R., et al. (2020). Did ice-charging generate volcanic lightning during the 2016–2017 eruption of Bogoslof volcano, Alaska? Bulletin of Volcanology, 82(3), 24. https://doi.org/10.1007/s00445-019-1350-5
- Van Eaton,, A. R., Smith,, C. M., Pavolonis,, M., & Said,, R. (2022). Eruption dynamics leading to a volcanic thunderstorm—The January 2020 eruption of Taal volcano, Philippines. *Geology*, 50(4), 491–495. https://doi.org/10.1130/G49490.1
- Walker,, G. P. L., & Croasdale,, R. (1971). Characteristics of some basaltic pyroclasts. Bulletin of Volcanology, 35(2), 303–317. https://doi.org/10.1007/BF02596957
- Wilson,, L., & Huang,, T. C. (1979). The influence of shape on the atmospheric settling velocity of volcanic ash particles. Earth and Planetary Science Letters, 44(2), 311–324. https://doi.org/10.1016/0012-821X(79)90179-1
- Wilson,, L., Sparks,, R. S. J., Huang,, T. C., & Watkins,, N. D. (1978). The control of volcanic column heights by eruption energetics and dynamics. *Journal of Geophysical Earth: Solid Earth*, 83(B4), 1829–1836. https://doi.org/10.1029/JB083iB04p01829
- Wohletz,, K., Zimanowski,, B., & Büttner,, R. (2013). Magma-water interactions. In S. Fagents, T. Gregg, & R. Lopes (Eds.), Modeling volcanic processes: The physics and mathematics of volcanism (pp. 230–257). Cambridge University Press. https://doi.org/10.1017/CB09781139021562.011
- Wohletz., K. H. (1983). Mechanisms of hydrovolcanic pyroclast formation: Grain-size, scanning electron microscopy, and experimental studies. Journal of Volcanology and Geothermal Research, 17(1–4), 31–63. https://doi.org/10.1016/0377-0273(83)90061-6
- Woods,, A. W., & Self., S. (1992). Thermal disequilibrium at the top of volcanic clouds and its effect on estimates of the column height. *Nature*, 355(6361), 628–630. https://doi.org/10.1038/355628a0
- Zimanowski,, B., Büttner,, R., & Lorenz,, V. (1997). Premixing of magma and water in MFCI experiments. *Bulletin of Volcanology*, 58(6), 491–495. https://doi.org/10.1007/s004450050157

References From the Supporting Information

Rudlosky,, S. D., Goodman,, S. J., Virts., K. S., & Bruning,, E. C. (2019). Initial geostationary lightning mapper observations. *Geophysical Research Letters*, 46(2), 1097–1104. https://doi.org/10.1029/2018GL081052

CAHALAN ET AL. 23 of 23